

Simulation of the EXILL detector array and analysis of the continuum region in the neutron capture reaction on ^{77}Se

MASTER-ARBEIT

zur Erlangung des akademischen Grades

Master of Science
(M.Sc.)

vorgelegt

der Fakultät Mathematik und Naturwissenschaften
der Technischen Universität Dresden

von

Christian Lorenz B.Sc.

geboren am 01.09.1989 in Dresden

Eingereicht am : 20. November 2014

Die Master-Arbeit wurde in der Zeit von Oktober 2013 bis November 2014 im
Institut für Strahlenphysik, Helmholtz-Zentrum Dresden-Rossendorf
angefertigt.

1. Gutachter: Prof. Dr. Thomas E. Cowan
Helmholtz-Zentrum Dresden-Rossendorf und
Technische Universität Dresden
t.cowan@hzdr.de

2. Gutachter: PD Dr. Daniel Bemmerer
Helmholtz-Zentrum Dresden-Rossendorf
d.bemmerer@hzdr.de

- Betreuer: Dr. Ronald Schwengner
Helmholtz-Zentrum Dresden-Rossendorf
r.schwengner@hzdr.de

Summary

The neutron-capture reaction with cold neutrons on a highly enriched ^{77}Se target has been performed in the course of the EXILL campaign at the high-flux reactor of the Institut Laue-Langevin Grenoble. The compound nucleus ^{78}Se formed by the neutron capture is left in an excited state and de-excites via the emission of gamma-ray cascades. Using the multi-detector array EXILL it is possible to analyze coincidences and investigate the nuclear structure of ^{78}Se . To allow the determination of absolute physical quantities, a detector simulation of the complete EXILL array with Geant4 has been developed and evaluated. The detector response has been deduced and the measured spectra were unfolded. After an efficiency correction, the response corrected spectra have been compared with simulated spectra using the statistical gamma-cascade computer code γDex to determine strength functions. An analysis of coincidence spectra could not be performed, due to inconsistencies in the recorded raw data. This problem suggested substantial corrections of the data processing, which are subject of subsequent work.

Zusammenfassung

Im Rahmen der EXILL-Kampagne am Hochflussreaktor des Instituts Laue-Langevin in Grenoble wurde die Neutroneneinfangsreaktion an hoch angereichertem ^{77}Se untersucht. Der durch den Neutroneneinfang erzeugte Verbundkern ^{78}Se befindet sich nach der Reaktion in einem angeregten Zustand und regt sich unter der Ausstrahlung von Gammakaskaden bis zum Grundzustand ab. Mit Hilfe des EXILL Detektoraufbaus ist es möglich, Koinzidenzereignisse zu analysieren und die Kernstruktur von ^{78}Se zu untersuchen. Um auch absolute physikalische Größen zu bestimmen, wurde mit Geant4 eine Simulation des EXILL Detektoraufbaus entwickelt und evaluiert. Anschließend wurde sie genutzt, um die Detektorantwortfunktion zu bestimmen und die gemessenen Spektren zu entfalten. Die entfaltenen und effizienzkorrigierten Spektren wurden mit simulierten Spektren des statistischen Gammakaskaden-Simulationsprogramms γDex verglichen, um Rückschlüsse auf Stärkefunktionen schließen zu können. Eine Analyse von Koinzidenzspektren konnte aufgrund von Unstimmigkeiten in den aufgenommenen Rohdaten nicht durchgeführt werden. Dieses Problem erfordert eine grundlegende Korrektur in der Bearbeitung der Rohdaten, welche Inhalt weiterführender Arbeiten sein wird.

Contents

1	Introduction and Motivation	1
2	Theoretical Background	3
2.1	Neutron Capture Reaction	3
2.2	De-excitation via Gamma Rays	4
2.3	Concept of Average Radiation Widths	6
2.3.1	Strength Functions	7
2.3.2	Level Density	8
2.4	Detector Response & Efficiency	9
3	Experimental Setup	13
3.1	ILL Grenoble & the PF1b Experimental Area	13
3.2	EXILL Detector Array	14
4	EXILL Simulation	17
4.1	Geometry	18
4.1.1	EXOGAM	18
4.1.2	GASP	20
4.1.3	LOHENGRIN	21
4.2	Response & Efficiency	22
4.3	Evaluation	25
4.4	Discussion	29
4.4.1	Detector Resolution	29
4.4.2	Dead Layer	30
5	Analysis	33
5.1	Detector Efficiency	38
5.2	Response Correction	40
5.3	Coincidence Analysis	45
5.4	Strength Function	47
6	Results, Discussion and Outlook	51
A	Appendix	53
	Literature	55

1 Introduction and Motivation

In 1932, a scholar of Ernest Rutherford – James Chadwick – discovered the existence of a new, uncharged particle: the neutron. Inspired by the newly found particle, Enrico Fermi bombarded thorium and uranium, the heaviest elements known at the time, with neutrons and observed for the first time what became to be known as nuclear fission – one of the most important principles the modern energy production is based on.

Nuclear power provides about a third of the electrical energy consumed in the European Union. Although nuclear power can compete with other renewable power generation sources in terms of the emission of greenhouse gases, it has one major drawback: the production of radioactive nuclear waste.

Nuclear waste comprises many short and long-lived isotopes, whereby the latter will be hazardous for at least 10^5 years. So far nuclear waste is stored underground but there are concepts to reduce the long storage time by reprocessing the nuclear waste. The current approach is the transmutation of the long-lived into short-lived isotopes via nuclear reactions.

However, to build and run future facilities for transmutation of nuclear waste, complex and extensive simulations of the processes happening during the transmutation have to be made. In order to do so, many properties, such as cross sections for photonuclear and neutron induced reactions, of the participating nuclei have to be taken into account. In contrast to long-lived isotopes, short-lived ones are experimentally inaccessible. Hence, their properties have to be calculated by means of theoretical models.

The task of the scientific community is to elaborate these theoretical models. In particular there are two important quantities which many models use as an input: the photon strength function and the nuclear level density.

The experiment which is subject of this thesis, is one in a series of experiments with the aim to investigate general properties of the photon strength function. In 2009 and 2010 two twin experiments were conducted: first neutron capture experiments on ^{77}Se and ^{195}Pt at the research reactor of the Hungarian Academy of Sciences in Budapest, and subsequently photon scattering experiments on ^{78}Se and ^{196}Pt at Helmholtz-Zentrum Dresden-Rossendorf. Their aim was to compare the experimental strength functions of the same nucleus deduced from two different reactions (inelastic photon scattering and neutron capture) [Schr 12].

The combination of the investigated nuclei is crucial for that purpose:

Nuclei like ^{78}Se with an even number of protons and neutrons have a 0^+ ground state. After an excitation via inelastic photon scattering mostly 1^- states are populated. To excite a comparable 1^- state after a neutron capture reaction, the target nucleus (in this case ^{77}Se) has to have a $\frac{1}{2}^-$ ground state. Only a few combinations of stable nuclei with this property exist on the nuclear chart, where (^{77}Se , ^{78}Se) and (^{195}Pt , ^{196}Pt) are two of them.

In addition, ^{77}Se is very similar to ^{79}Se , which is a long-lived fission product. This isotope is very volatile, which causes serious issues during the nuclear waste storage.

To understand the nature of strength functions better, it is of particular interest to see whether the strength function is the same for a de-excitation to the

ground state and for a de-excitation to the first or second excited state. Therefore, a multi-detector array is needed in order to distinguish between those transitions by performing coincidence analysis. The aforementioned experiments have been conducted with only one detector, but within the scope of the EXILL campaign at the ILL Grenoble in 2012 a detector array has been assembled, which covers the needs of such a coincidence analysis.

With the same ^{77}Se target that was used for the experiment at the research reactor in Budapest, 393.4 GB of data of the $^{77}\text{Se}(n,\gamma)^{78}\text{Se}$ reaction have been recorded during 3 days of beam time at the ILL reactor. In [John 14] the level scheme of ^{78}Se was extended and newly found transitions have been reported and placed within the scheme.

The present work aims primarily at the development of a detector simulation of the EXILL detector array in order to deduce its detector response. The detector response is needed for any determination of absolute quantities, e. g. cross sections and the related strength functions. In this thesis it is used in particular to access the quasi-continuum of emitted gamma rays. Furthermore, a coincidence analysis has been performed with the goal to deduce strength functions on excited states.

2 Theoretical Background

Similar to the atomic shell, a nucleus consisting of nucleons (protons and neutrons) can be excited to higher lying states which can be formed of singly excited nucleons but also of many collectively excited nucleons. Such excitations occur after a stimulation with an electromagnetic field, radioactive decays or nuclear reactions, such as heavy-ion collisions, alpha-particle induced reactions, proton or neutron capture and scattering. An excited nucleus always tends to de-excite to its ground state. It is the quantum mechanical nature and its respective rules that govern that process: Particle emission (protons, neutrons or alpha particles), fission, β -decay and emission of electromagnetic radiation “gamma rays” are the most important ones. Since this work is based on a neutron-capture reaction followed by de-excitation via gamma rays, these processes are discussed in more details in sections 2.1 and 2.2. Consecutively, section 2.3 addresses the quantities *strength function* and *level density*, as they are needed to describe the nucleus and its de-excitation via gamma rays on a statistical basis.

2.1 Neutron Capture Reaction

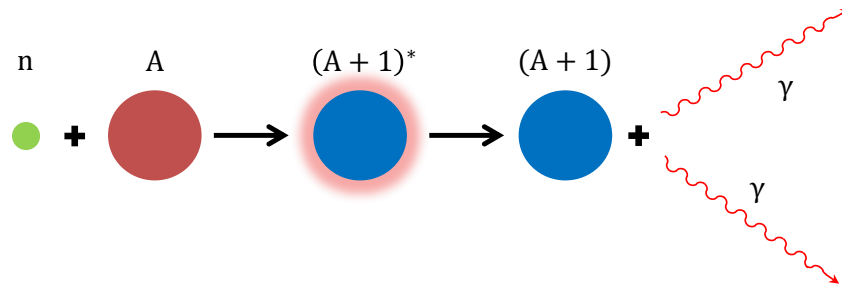


Figure 2.1 – Pictorial view of the neutron-capture reaction. The target nucleus captures a neutron and forms an excited compound nucleus, which then de-excites via gamma-ray emission.

A simple scheme of a neutron-capture reaction is shown in figure 2.1. First a neutron n is captured by a target nucleus (mass number A , proton number Z), forming a compound nucleus $(A + 1, Z)$. During the capture process the neutron-separation energy S_n is released, hence the compound nucleus is excited with an energy E_{ex} , according to equation (2.1), where T_n is the kinetic energy of the neutron and E_R the recoil energy of the compound nucleus.

$$E_{\text{ex}} = S_n + T_n - E_R \quad (2.1)$$

As the spin parity of the neutron is $\frac{1}{2}^+$, the compound nucleus can be in a state of $|J_T \pm \frac{1}{2}|^{\Pi_T}$. Here $J_T^{\Pi_T}$ stands for the spin parity of the target nucleus’ ground state. In the present work cold neutrons were impinged on a ^{77}Se target, following the reaction $^{77}\text{Se}(n,\gamma)^{78}\text{Se}$. The kinetic energy of the neutrons was $T_n \sim 5$ meV, which is

many orders below the neutron-separation energy of ^{78}Se : $S_n = 10497.73 \pm 0.17$ keV [ENSDF]. Thus T_n can be neglected in equation 2.1 as well as E_R due to the larger mass of ^{78}Se compared to that of a neutron. Therefore, the energy E_{ex} of the excited nucleus is approximately S_n . Possible spin parities of the excited state are 1^- and 0^- as the ground state of ^{77}Se has a spin parity of $\frac{1}{2}^-$. For these reasons only states very close to S_n can be excited, which is dominantly the 1^- state 41 eV below the neutron-separation energy according to [Mugh 06]. It is energetically possible to emit either a proton or a neutron, because the excitation energy is right at the neutron-separation energy and above the proton-separation energy which is $S_p = 10398.40 \pm 0.18$ keV [ENSDF]. However, it appears that the de-excitation by emission of gamma rays is strongly preferred. The energetics of the whole process is illustrated in figure 2.2.

2.2 De-excitation via Gamma Rays

When a nucleus de-excites from a state λ to a state δ by emission of a gamma ray, a part of their energy difference is carried away by the gamma ray, the other part is carried away as recoil energy by the nucleus itself. Typical gamma-ray energies range from keV to tens of MeV. Since the rest energies of nuclei are much greater (in case of ^{78}Se it is ~ 73 GeV) it can be calculated that the recoil energy takes less than a percent, using energy and momentum conservation. The detector resolution is usually much worse than that and the recoil energy does not need to be taken into account.

Electromagnetic radiation can be characterized by its angular momentum L and its parity. The angular momentum defines the multipole order of the radiation which is *dipole* radiation in case of $L = 1$, *quadrupole* radiation in case of $L = 2$, and so on. The parity in combination with the multipole order determines the nature of the radiation, which can be either of *electric* or of *magnetic* type. Together it is denoted as XL where X stands for E (*electric*) or M (*magnetic*). Table 2.1 gives an overview of the first two multipole orders and the quantum mechanically forbidden transitions. Higher multipole orders are usually negligible as the transition probability decreases with a factor $\sim 10^{-4}$ [Maye 02] with each higher order in multipole radiation. Furthermore, the magnetic multipole radiation is usually one or two orders less probable than the electric multipole radiation.

radiation type	E1	M1	E2	M2
order		dipole		quadrupole
final state parity Π_δ	$-\Pi_\lambda$	Π_λ	Π_λ	$-\Pi_\lambda$
final state spin J_δ	$ J_\lambda - 1 \leq J_\delta \leq J_\lambda + 1$		$ J_\lambda - 2 \leq J_\delta \leq J_\lambda + 2$	
forbidden spin transitions	$0 \rightarrow 0$		$0 \rightarrow 0, 0 \rightarrow 1, \frac{1}{2} \rightarrow \frac{1}{2}$	

Table 2.1 – Characteristics of the first two multipole orders for a transition from an initial state λ to a final state δ .

During a de-excitation the parity and angular momentum must be conserved. This restricts the possible combinations of multipole radiation and final state, depending on the spin and parity of the initial state. If a nucleus undergoes a de-excitation via a cascade of gamma-ray transitions then the first emitted gamma ray defines a spatial orientation of the nucleus. The following gamma rays of the cascade are emitted with an angular correlation relative to the first gamma ray. The underlying angular distribution is exclusively connected to the type of the multipole radiation of each gamma-ray transition.

Measuring the gamma-ray energy and angular distributions are just two of several methods to get information about the energy and spin parity of the nucleus' levels. Furthermore, measuring partial radiative widths from a certain state to lower lying states can reveal the nature of the excitation (e.g. rotation or vibration of the nucleus).

Obviously the gamma spectrum measured in an experiment is a fingerprint of the

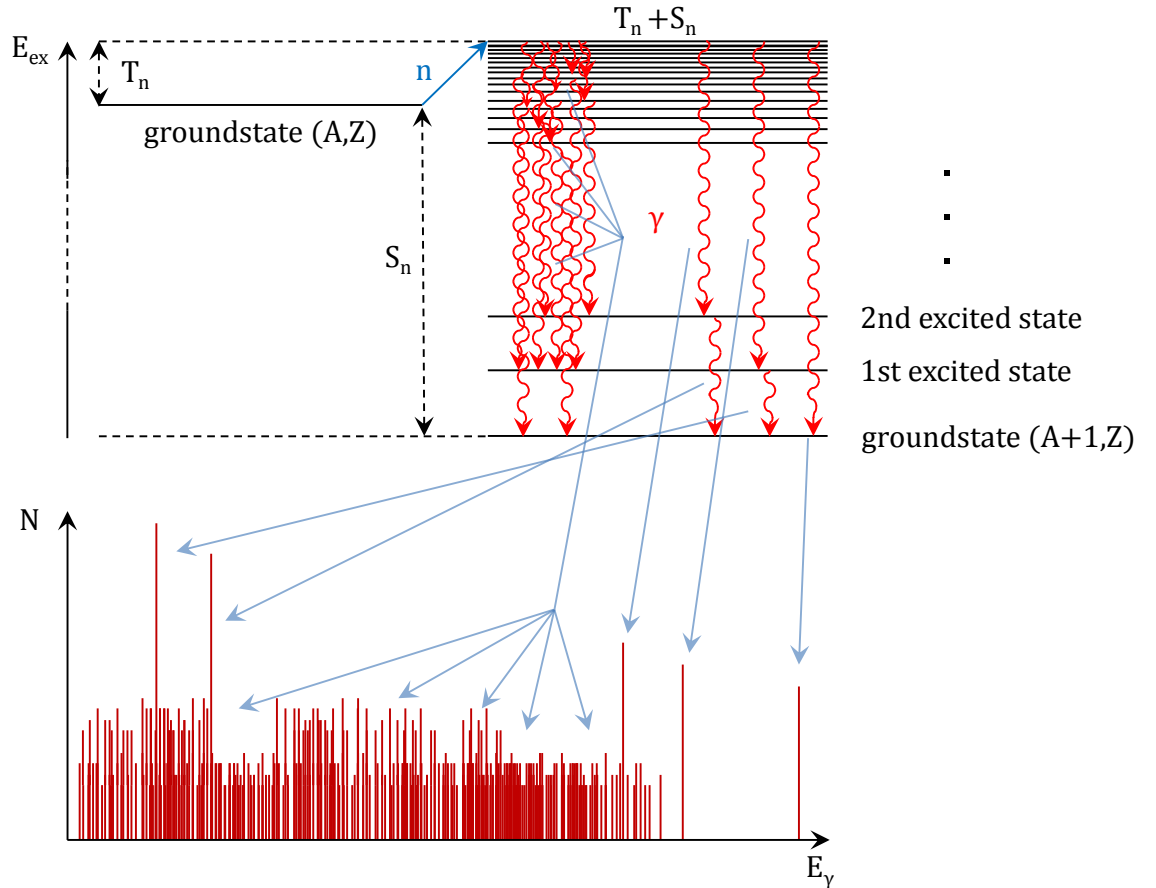


Figure 2.2 – Scheme of the energetics of the neutron-capture reaction and the origin of different structures in the gamma-ray spectrum. After the target nucleus (A, Z) (top left) captured a neutron, the compound nucleus $(A + 1, Z)$ (top right) is excited by the released neutron-separation energy S_n plus the neutron's kinetic energy T_n (neglecting the recoil energy). The de-excitation to the ground state via gamma rays leads to characteristic gamma spectra with strong peaks in the low and high energy part of the spectrum and to a quasi-continuum in the intermediate part (further explanation is given in the text).

nuclear structure of the investigated nucleus. However, as indicated in figure 2.2, low lying states are well separated, whereas with higher excitation energy the level distance gets smaller. This leads to well separated peaks at the high energy part of the spectrum resulting from transitions from the capture state to the ground state and lowest excited states. In the low energy part of the spectra very strong peaks appear due to the de-excitation of the low lying states to the ground state. The intermediate part is formed by the so-called quasi-continuum, which is composed of many weak gamma peaks. Their origin is a transition from or to states of higher energies where the level density is very high. The finite detector resolution (see section 2.4) makes it impossible to resolve those gamma peaks, hence they appear as a continuum.

On the one hand the clearly visible and strong discrete peaks in the high-energy and low-energy part of the spectrum give comparatively easy access to the spin parity, energy and radiative widths of the low lying states of the nucleus using angular correlation, peak intensity and coincidence measurements. On the other hand it is impossible to get precise information about each single state at higher energies, because the methods applied to single peaks are not applicable to the quasi-continuum. Not only the experimental access to those states is hindered, but also their theoretical description is almost impossible, as the nucleus is a complex many-body system which still cannot be solved accurately enough to give detailed predictions.

The way out is to treat those states in a statistical manner instead of each of them individually. This leads to the concept of *strength functions* and *level densities* to calculate average radiation widths which will be discussed in the section 2.3.

2.3 Concept of Average Radiation Widths

The lifetime τ_λ of a certain state in a nucleus can be related to its total width Γ_λ via the uncertainty principle:

$$\Gamma_\lambda \cdot \tau_\lambda = \hbar \quad (2.2)$$

The total width itself is the sum of partial widths of all possible decays the excited nucleus can undergo. This includes the width of decays with particle emission Γ_x (e. g. protons, neutrons, α -particles) and partial radiation widths of de-excitations to lower states δ via gamma radiation $\Gamma_{\lambda\delta}$:

$$\Gamma_\lambda = \sum_{\delta} \Gamma_{\lambda\delta} + \Gamma_x \quad (2.3)$$

As stated in previous section 2.1, individual partial radiation widths for a decay from a state λ to a state δ ($E_\delta < E_\lambda$) are experimentally and theoretically inaccessible (except for low lying states). Nevertheless, one can formulate an average radiation width $\bar{\Gamma}_{\delta\lambda XL}^J$ for a de-excitation via gamma radiation of multipole type XL from a number of levels with spin parity J within an interval around the fixed excitation energy E_λ to a state at E_δ [Bart 73]:

$$\bar{\Gamma}_{\delta\lambda XL}^J = \frac{f_{\delta\lambda XL}^J(E_\gamma) E_\gamma^{2L+1}}{\varrho_J(E_\lambda)} \quad (2.4)$$

The average radiation width is based on the quantities strength function $f_{\delta\lambda XL}^J$ and

level density ϱ_J . Both are explained in more detail in the sections 2.3.1 and 2.3.2. The spectral distribution of emitted gamma rays (multipole type XL) coming from states with spin parity J in an interval around E_λ and decaying to states with spin parity I in an interval around $E_\delta = E_\lambda - E_\gamma$ is then given by:

$$\nu_{\delta\lambda XL}^J(E_\gamma) = \frac{\bar{\Gamma}_{\delta\lambda XL}^J \sum_I \varrho_I(E_\lambda - E_\gamma)}{\bar{\Gamma}_{\text{Tot}\lambda}^J} \quad (2.5)$$

$$= E_\gamma^{2L+1} \frac{f_{\delta\lambda XL}^J(E_\gamma)}{\bar{\Gamma}_{\text{Tot}\lambda}^J} \frac{\sum_I \varrho_I(E_\lambda - E_\gamma)}{\varrho_J(E_\lambda)} \quad (2.6)$$

where $\bar{\Gamma}_{\text{Tot}\lambda}^J$ is the average total width. The sum \sum_I covers all those I that can be reached by a radiation of multipole XL from states of spin parity J (see table 2.1). As $\bar{\Gamma}_{\text{Tot}\lambda}^J$ and $\varrho_J(E_\lambda)$ do not depend on E_γ , the slope of the spectra only depends on the strength function and the level density at E_δ . Hence, these two quantities are the key to describe the continuum part of gamma spectra, which motivates deeper experimental investigation in order to get better constraints on the models predicting them.

Unfortunately it is not possible to extract $\nu_{\delta\lambda XL}^J(E_\gamma)$ from the conducted neutron-capture experiment at EXILL. Instead, the measured spectrum is the sum of the contributions from all states λ that are populated during a cascade and all possible radiation types XL . However, using the *Spectrum Fitting Method* as described in [Bart 73] it is still possible to restrain the models predicting strength function and level density:

With different trial strength functions and level densities the expected spectral shape is simulated and compared with the observed shape. The simulation used within this work is done with the computer code γDex [Schr 12] [Mass 14] [Maki 14].

It should be emphasized that the statistical approach is based on the assumption that the intervals around E_λ and E_δ are chosen large enough to contain a statistically representative set of levels. Therefore, the bin width of the simulated and observed spectra must be large enough as well (e. g. 100 keV).

2.3.1 Strength Functions

The strength function $f_{\delta\lambda XL}^J$, as it is introduced in equation 2.4, depends on the radiation type XL and energy E_γ , on the spin parity and energy E_λ of the initial state. However, based on [Brin 55] and [Axel 62] it has been formulated what is often referred to as the Axel-Brink hypothesis [Bart 73]: it is assumed that the $E1$ strength function is the same for photon excitation and de-excitation and it does not depend on the detailed structure of the initial state. Often it is assumed that this statement is valid for any multipole type XL . Furthermore, it has been predicted (see [Bart 73] and references therein) that the strength function is independent of J .

This means that the strength function does only depend on the multipole type and the energy of the emitted radiation:

$$f_{\delta\lambda XL}^J(E_\gamma) \rightarrow f_{XL}(E_\gamma) \quad (2.7)$$

For the most important radiation types $E1$, $M1$ and $E2$ many models have been proposed. In the following the strength functions used by γ Dex are shortly discussed:

- The $E1$ strength function is dominated by the so-called ‘‘Giant Dipole Resonance’’ (GDR) with a broad maximum around 12 to 16 MeV. It is well studied for many nuclei and it was found that a description with one Lorentzian for spherical nuclei and two Lorentzians for deformed nuclei is reasonable ([Axel 62] & [Kope 93]). Free parameters are deduced by fits to measured data and are evaluated in [RIPL3]. In [Jung 08] another description with only two parameters based on three Lorentzians (TLO) is suggested, which describes a wide range of nuclei of different shape fairly well. The Lorentzians account for the deformation along three spatial axis, supporting the description of a triaxial deformed nucleus. γ Dex offers the possibility to choose from either of these options.
- The $M1$ strength function is represented by the sum of three Gaussians associated with the scissors mode, an isoscalar and an isovector spin-flip mode [Heyd 10]. Their individual parameters are described in [Schr 11] and [Schr 12].
- Following the [RIPL3] recommendation, the $E2$ strength function is taken to be one Lorentzian.

2.3.2 Level Density

In addition to strength functions, the level density is an important statistical property of the nucleus to calculate for example the spectral distribution of gamma rays (2.5) in section 2.3. The level density $\varrho_J(E)$ describes the number of states with spin parity J within an interval around the excitation energy E . A common ansatz is to write $\varrho_J(E)$ as a product of a parity distribution, a spin distribution and the total level density. The models and its parameters used in the γ Dex code are well described in [Schr 12] and [Mass 14].

The parity distribution is taken from [Al Q 03], which predicts an equal distribution of positive and negative parities at energies above about 3 MeV. For the spin distribution the recommendation given in [Egid 09] is used. The parameters of the spin and parity distribution are either fixed or tabulated for different nuclei. The deuteron pairing energy which occurs in the model of the spin distribution is 2.937 MeV for ^{78}Se (see [Egid 09], [Egid 05] and [Audi G 04]).

As supported in [Schm 11] the Constant Temperature Model (CTM) [Gilb 65] is used to describe the total level density. There the total level density is predicted to have an exponential behavior:

$$\varrho_{tot}(E) = \frac{1}{T} e^{\frac{E-E_0}{T}} \quad (2.8)$$

The two parameters T and E_0 are the temperature and back-shift energy, respectively. In [Egid 09] and [Koni 08] for many nuclei T and E_0 are listed, which vary especially in E_0 . As the γ Dex code follows [Egid 09], the values therein are used: $T = 0.89 \pm 0.03$ MeV and $E_0 = -0.04 \pm 0.26$ MeV.

2.4 Detector Response & Efficiency

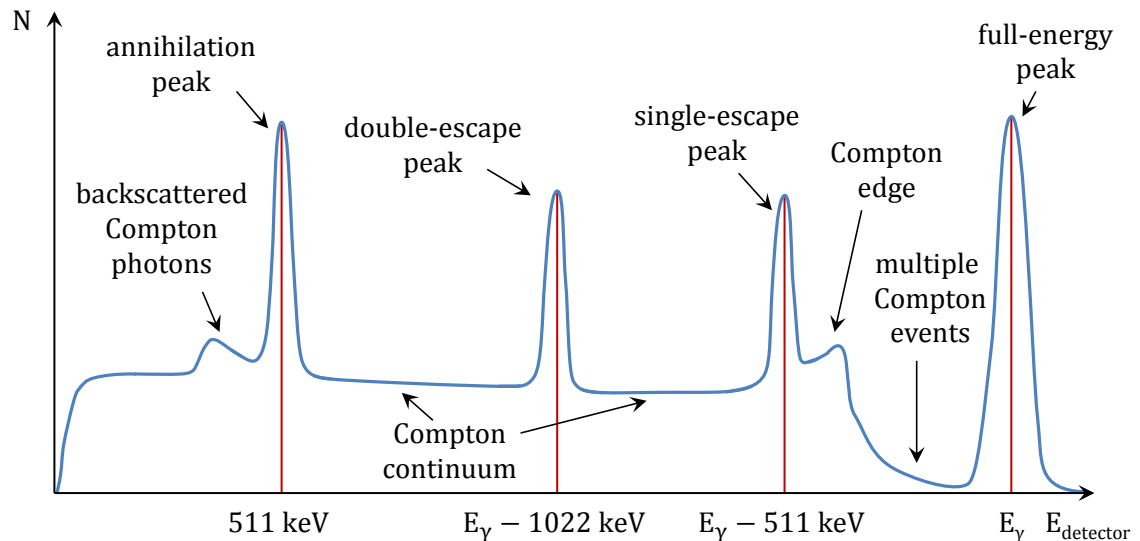


Figure 2.3 – Scheme of the characteristic features of a detector response. For gamma-ray energies below 1022 keV, the escape peaks vanish.

Although gamma rays emerging from a de-exciting nucleus have a well defined energy, the gamma-ray spectrum measured with a detector does not show only single narrow peaks at the corresponding gamma-ray energy. Instead, broadened peaks and additional features like annihilation, single and double-escape peaks and Compton continuum (see figure 2.3) are observed. These structures reflect the types of interaction of photons with matter. Together they form what is called the detector response.

The detection process can be separated into the interaction of a gamma ray with an electron of the detector material, which leads to an electron-hole pair, and the electromagnetic shower caused by that electron-hole pair.

In the first part of the detection process there are mainly three possible interaction mechanisms: photoelectric absorption, Compton scattering and pair production. The former leads to a signal directly proportional to the incident gamma energy, as it transfers all its energy E_γ to the electron. This results in a photo peak in the measured spectrum.

If just a portion of the photon's energy is transferred to the electron, the remaining energy is carried away by the scattered photon. This interaction is called Compton scattering and well described by the Klein-Nishina formula [Klei 28]. The outgoing photon eventually undergoes any of the three mentioned processes in the same crystal, in other parts of the detector or in other detectors if present. Due to this interaction, a Compton continuum appears from zero energy up to the Compton edge, which is the maximum energy a photon can transfer to the electron by scattering at an angle of 180° . By scattering multiple times, an incident photon can also deposit more energy in the detector volume, than it would by scattering at an angle of 180° . If a photon undergoes Compton scattering at backward angles in any material surrounding the detector, the scattered photon might be detected by the detector. This leads to an additional bump in the detector response (backscattered Compton photons).

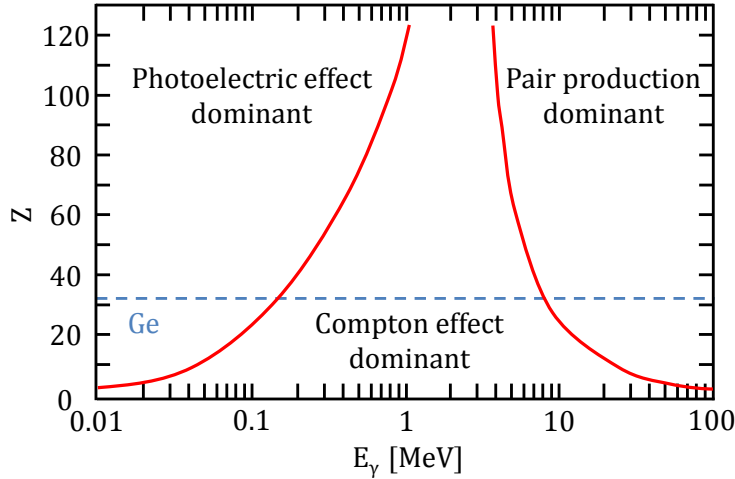


Figure 2.4 – The dominant interaction mechanisms of photons with matter as function of the photon energy and the proton number Z of the material. For germanium Z is 32, which is indicated with the blue line. (Figure inspired by [Evan 72])

The third important interaction – the pair production – leads to formation of additional peaks beside the full-energy peaks. In the strong coulomb field of a nucleus, the incident gamma ray can convert its energy into an electron-positron pair, which will produce an electromagnetic shower. The positron will at some point annihilate with an electron, creating two 511 keV photons. If one or both of these photons escape the detector volume without any interaction, then the measured signal corresponds to an energy of $E_\gamma - 511$ keV or $E_\gamma - 1022$ keV which leads to a single and a double-escape peak, respectively. Furthermore, these 511 keV photons might be detected by another detector, resulting in the annihilation peak at 511 keV. The pair production obviously requires the incident gamma ray to have an energy larger than 1022 keV to produce the electron-positron pair. Therefore, this process becomes a significant interaction mechanism if the gamma energy is in the order several MeV or larger (see figure 2.4).

The full-energy peak is the sum of the photo peak and those events, where no scattered photons or photons produced via pair production escaped the detector volume.

The second part of the interaction determines the peak shape and depends on the detector properties. The present experiment was conducted only with HPGe detectors. Their main component is a high-purity germanium crystal with an electrode in the center and another one at the outer surface. When operated at the temperature of liquid nitrogen and under high voltages (kV), a large depleted zone where no charge carriers are available is created. The electron-hole pair created by the incident gamma ray transfers its energy to other electrons and many charge carriers (electron-hole pairs) are produced. Due to the strong electric field, they will drift to the electrodes of the detector, where a measurable electric current is induced. This electrical current is proportional to the number of the charge carriers produced, which in turn is of statistical nature. For this reason the peaks are broadened and have a gaussian shape. It may happen that some of the charge carriers recombine on their way to the electrode due to impurities in the crystal. This is more often

the case with the holes drifting towards the cathode, because they have a lower drift velocity. This effect leads to the appearance of a tail at the low-energy side of the peak. These two processes (statistical nature of the number of charge carriers and the recombination) have the largest impact on the peak shape. They strongly depend on the shape of the crystal, its level of purity and the electric field within the crystal.

Obviously it is an ambitious task to correct a measured spectrum for the detector response. Not only the underlying processes are complex, but also the scattering of gamma rays from objects surrounding the detector arrangement or from detector volumes into other detector volumes makes the determination of the detector response difficult.

Many algorithms and methods have been developed to estimate the detector response of different setups. Some methods which estimate the background (here background means everything in the spectrum that is not a peak) from the measured spectrum itself are described in [Burg 83], [Kawa 76] and [Gera 92]. However, they cannot make the distinction between the quasi-continuum (see section 2.2) and the Compton continuum. Hence, they are not applicable in this work.

Another method is proposed in [Radf 87]. With gamma-ray sources like ^{24}Na , ^{60}Co , ^{88}Y or ^{137}Cs , which are well known and decay via the emission of only a very few gamma rays, it is possible to measure the detector response at certain energies and extract its properties. Then one can extrapolate the detector response to other energies, which seems to be a very accurate method. As stated in their work, it is possible to measure the detector response within a range from 122 keV to 2.75 MeV with various sources. Based on that, they were able to estimate the detector response up to 5 MeV.

However, these measurements have not been done in the case of EXILL. Furthermore, in order to apply the aforementioned method to the experiment analyzed in this work, one would have to extrapolate the detector response from 2.75 MeV up to 10.5 MeV, which is a much larger interval compared to what is done in [Radf 87] and thus the uncertainties would be larger.

Another method, the simulation of the detector with a computer code became more and more refined and powerful with the increasing computer performance. The most popular simulation toolkits are [MCNP] and [Geant4]. The latter is used in this work to simulate the EXILL detector array (see section 4).

The efficiency of a detector is a characteristic property, which is strongly correlated to the detector response. In the following, efficiency refers to the full-energy efficiency ε_{FE} , which is the number N_{FE} of detected gamma rays in the full-energy peak divided by the number N_{source} of gamma rays emitted from the source during a measurement period T . Usually one uses calibration sources of an activity A_{source} where the relative intensities I are well known. Then the detector efficiency can be calculated as follows:

$$\varepsilon_{\text{FE}}(E_\gamma) = \frac{N_{\text{FE}}(E_\gamma)}{N_{\text{source}}(E_\gamma)} = \frac{N_{\text{FE}}(E_\gamma)}{A_{\text{source}} \cdot I(E_\gamma) \cdot T} \quad (2.9)$$

3 Experimental Setup

The conducted experiment was part of the EXILL (EXOGAM @ ILL) campaign at the Institut Laue-Langevin (ILL) in Grenoble in 2012 and 2013 during two reactor cycles. During the campaign fission of uranium and plutonium and (n,γ) -reactions as well as life times were studied.

This chapter provides an introduction to the high-flux reactor, the PF1B cold neutron facility at ILL and the EXILL detector array.

3.1 ILL Grenoble & the PF1b Experimental Area

With its high-flux reactor (see fig.3.1) the Institut Laue-Langevin can provide the highest continuous neutron flux worldwide. Hence, it is the favored location for any experiments based on neutrons.

The reactor supplies 34 experimental areas with neutrons of energies ranging from meV to eV and is operated with highly enriched ^{235}U .

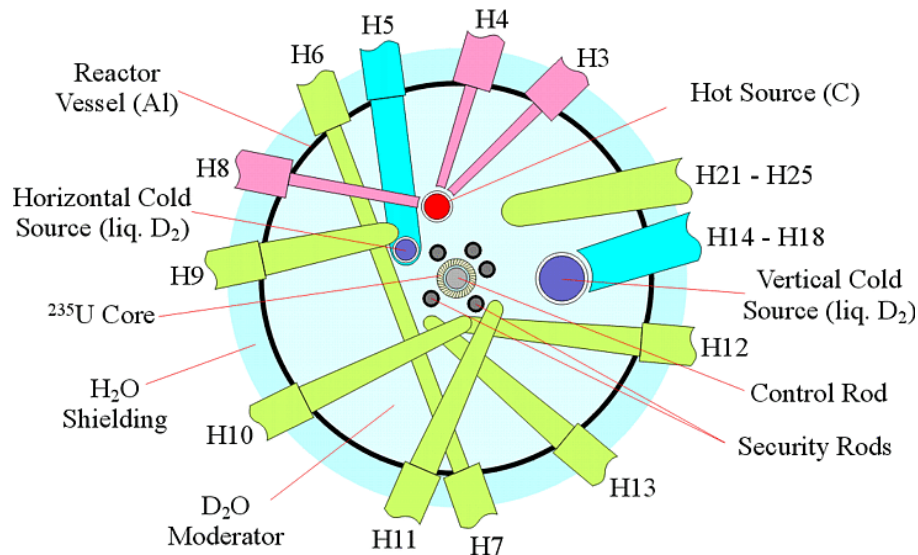


Figure 3.1 – Scheme of the reactor core, its sources and the neutron guides [ILL RE].

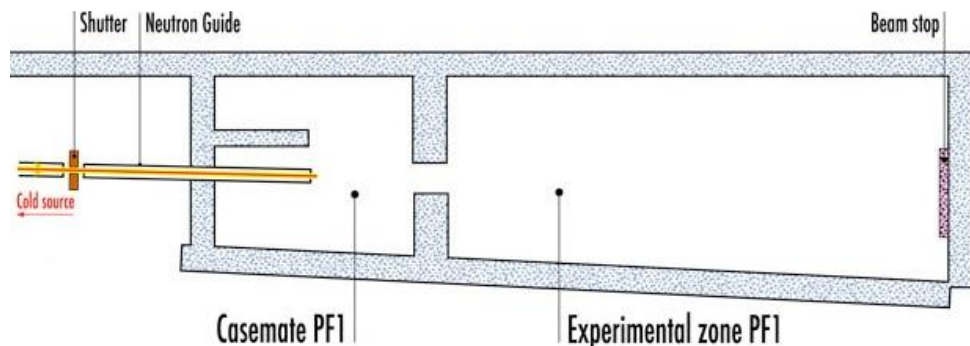


Figure 3.2 – Scheme of the PF1B facility [ILL PF1B].

In a pipe filled with liquid deuterium ($T = 25\text{ K}$) close to the reactor core, the moderated neutrons are further cooled down to energies of a few meV. These cold neutrons are delivered to the PF1B facility (see fig. 3.2) via the ballistic neutron super-mirror guide H113. There the EXILL detector array was assembled. The ballistic shape of the neutron guide is necessary as the neutrons are slow enough to be bent by the gravitational force. Additionally, it reduces the effect of background radiation originating from fast neutrons and gamma radiation produced in the reactor core. To avoid background radiation from neutrons interacting with the wall of the experimental hall and surroundings, and to allow a closely packed detector arrangement without harming the HPGe crystals due to neutron damage, the neutron beam was collimated using ceramic B_4C and plastic collimators backed with ${}^6\text{LiF}$ ceramic material as it is shown in figure 3.3. To absorb the photons produced in the collimators, they are additionally backed with lead. After the collimation the beam spot had a diameter of about 1 cm. Furthermore, the beam pipe and target chamber were kept under vacuum to reduce neutron scattering on air. Neutrons that did not interact with the target were stopped in a block of ${}^6\text{LiF}$ surrounded by lead, which was placed behind the detector array.

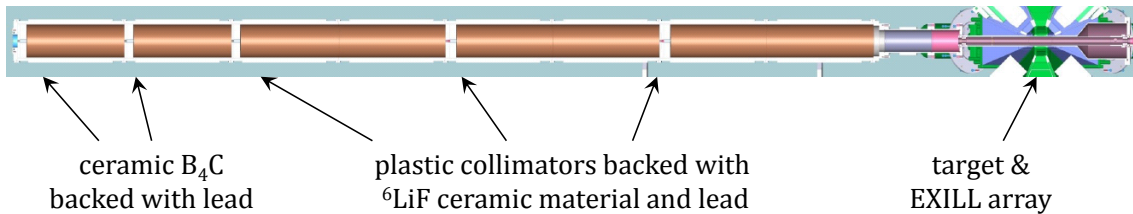


Figure 3.3 – Beam pipe and collimators [Mutt 13].

3.2 EXILL Detector Array

The EXILL detector array comprised 16 high-purity germanium (HPGe) detectors with a total number of 46 single crystals in the first part of the whole campaign (from October until December 2012).

Eight detectors were from the EXOGAM setup at GANIL [Simp 00]. The EXOGAM detectors are clover detectors consisting of 4 HPGe crystals in a common cryostat. Each of the individual crystals is segmented into 4 regions. However, the segmentation was not used during the campaign and only the core signal was recorded for each crystal. They were placed perpendicular to the beam pipe with an angle of 45° to the neighboring EXOGAM detectors, forming a ring around the target (see fig 3.5a).

Another two clover detectors were borrowed from the LOHENGRIN fission fragment spectrometer at the ILL. They were placed below the target at angles of 45° and 135° with respect to the beam (see fig 3.5c). The six remaining detectors were placed above and to the side of the target, again at an angle of 45° with respect to the beam (see fig 3.5b). They were provided by the Laboratori Nazionali di Legnaro (LNL) and were part of the former GASP array [Alva 93]. In contrast to the other detectors, they consist of a single crystal with a large volume.

The EXOGAM and GASP detectors were equipped with active anti-Compton shields, which were designed for the EXOGAM setup. They are composed of three parts at the side, rear side and backside of the cryostat (see fig. 4.3). The former two parts are made out of bismuth germanate (BGO) scintillator material whereas the latter is based on cesium iodide.

Furthermore, lead collimators were attached to the front of the side shields to prevent cross scattering between detectors as well as direct irradiation of the anti-Compton shields from the target. The intended use of the anti-Compton shields was to detect Compton scattered gamma rays exiting the detector volume. In the offline analysis it is then possible to reduce the Compton background of a detector by rejecting events in the HPGe detectors that are in coincidence with an event detected in the corresponding anti-Compton shield.

To get a sufficient rejection probability, one uses the aforementioned scintillator materials as their efficiency is higher than the efficiency of semiconductors.

As stated by [John 14] and other authors analyzing data from the EXILL campaign, the rejection of Compton-scattering events did not work in an optimum way. A reason might be a misalignment of the corresponding digitizer clocks. Although the anti-Compton shields could not be used as active veto shields, the cross scattering was reduced by their passive shielding.

The whole setup was mounted on an aluminum frame from the EXOGAM array.

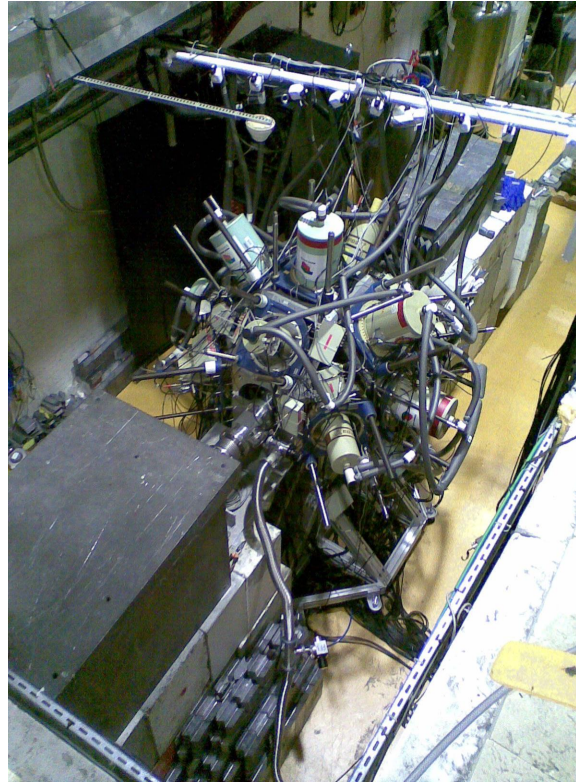


Figure 3.4 – The EXILL detector array at the PF1B facility.

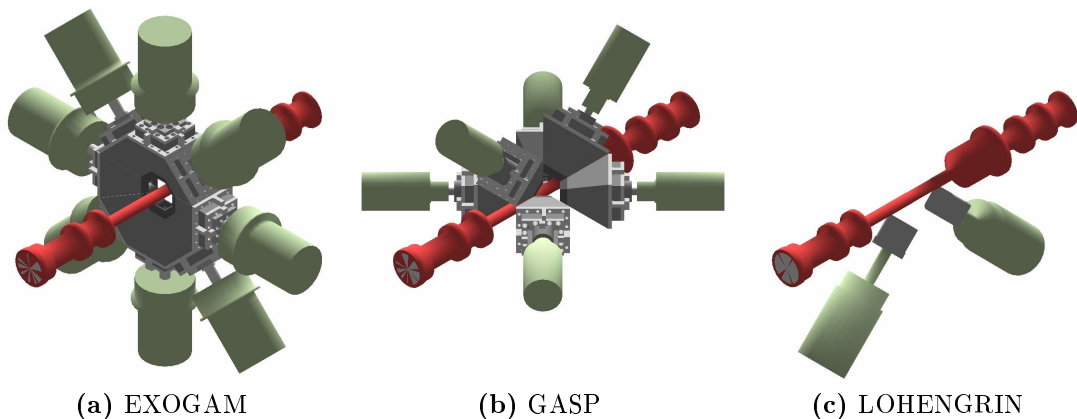


Figure 3.5 – Positions of the different detectors with respect to the beam pipe (shown in red). The neutron beam is coming from the left side.

For the data acquisition ten V1724, 8 channels 14 bit 100 MS/s CAEN digitizers were used to record the signals from the crystal cores and the anti-Compton shields. The recorded parameters are the uncalibrated energy, time and detector ID of each detected event. Hereby all events were recorded and no trigger was applied. All data processing was done offline after the experiment.

More detailed information about the data acquisition can be found in [Mutt 13]. A geometrical description of each detector and the array is given in section 4.1 where the simulation of EXILL with Geant4 is discussed.

Unfortunately, not all of the data taken during the $^{77}\text{Se}(n,\gamma)^{78}\text{Se}$ run are suitable for the analysis. One of the LOHENGRIN detectors had a malfunction and was removed from the array before the experiment. Furthermore, the remaining LOHENGRIN and the GASP detectors did not record events with energies above 6 to 7 MeV. As the excitation energy after the neutron capture is 10.5 MeV, the information between 6 and 10.5 MeV is missing, which makes a response correction as discussed in section 5.2 impossible. For this reason, the analysis focuses on the EXOGAM detectors.

4 EXILL Simulation

The development of a detector simulation of the EXILL array is the primary aim of the presented work. This simulation is crucial for the estimation of the detector response of the setup as other methods are not applicable (see section 2.4). In this chapter the implementation of the detector geometry and the simulated detector response and efficiency are presented. Subsequently, an evaluation of the simulation is discussed.

The whole simulation is carried out with [Geant4] (version 4.9.5p01). The detector geometry includes all detectors, beam pipe, aluminum frame and the target volume (see fig. 4.1). All detector parts can be switched on and off and important parameters (such as the distance from the target to the detectors) can be changed by interactive commands to easily adapt to different situations of the experiment or for testing purposes.

The target volume is different for each measurement during the EXILL campaign and therefore its size and position is adjustable by interactive commands as well. To account for an extended target the *GeneralParticleSource* class was used.

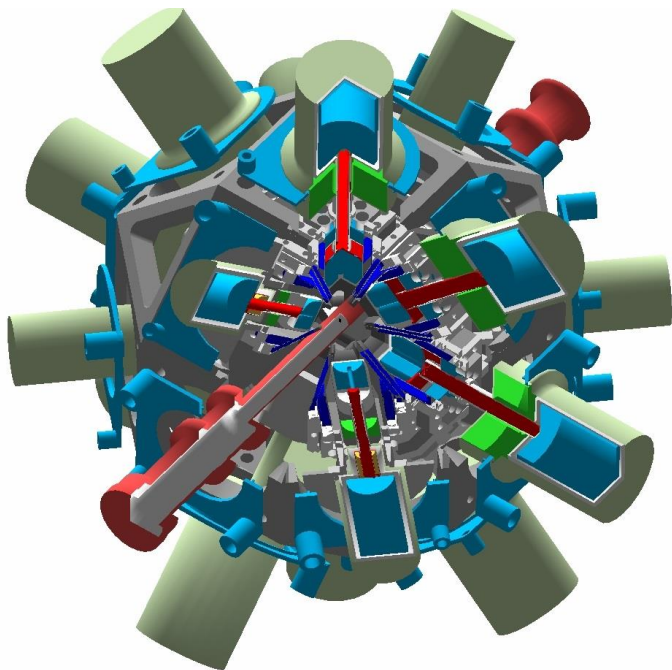


Figure 4.1 – The geometrical representation of EXILL detector array in Geant4.

In Geant4 the physics is handled by the *PhysicsList*. There are several standard compilations of models for the electromagnetic interactions provided by the Geant4 toolkit. For this simulation the *EmStandardPhysics_option3* was used. It is regularly used to validate Geant4 and designed for the simulation of electro-magnetic interactions with high accuracy. Two other recommended physics lists, *EmLivermorePhysics* and *EmPenelopePhysics*, have been tested but they did not lead to significantly different results.

The output is a ROOT-file [ROOT] which contains the spectra of all crystals and detectors with and without add-back (see section 5). Optionally one can also choose the output to be a list of all properties of each event.

4.1 Geometry

In the following subsections the different detector types and their geometries are outlined. The most time-consuming task was to build a detailed geometrical representation of the EXILL array in Geant4. Therefore, efforts have been made to collect the needed information from both the EXILL community, as well as the detector manufacturing companies. The only EXILL specific information about the arrangement and distances of the different array components is a CAD-file provided by M. Jentschel from ILL [Jent M]. All dimensions of the beam pipe and the mounting plates are taken therefrom. The target-to-detector distances cannot be retrieved from that file because they are inconsistent and lead to geometrical overlap.

4.1.1 EXOGAM

As was already pointed out in section 3.2, the EXOGAM detectors are the most important part of the array for the analysis. Each of them consists of four crystals cut out of a HPGe-cylinder, 90 mm in length and 60 mm in diameter. At the front side they are tapered for 30 mm with an angle of 22.5° at two adjacent faces as it is shown in figure 4.2. In the center there is a hole with a diameter of ~ 1 cm for the core electrode. The four crystals are located within one cryostat and held by a copper clamp at the backside of the crystals. A thick copper rod (~ 4.5 cm in diameter) connects the cryostat with the dewar. The BGO and CsI crystals of the anti-Compton shields at the side, rear side and backside of the cryostat have a thickness of ~ 1.0 , 2.1 and 3.8 cm, respectively. An overview of all different parts is shown in figure 4.3.

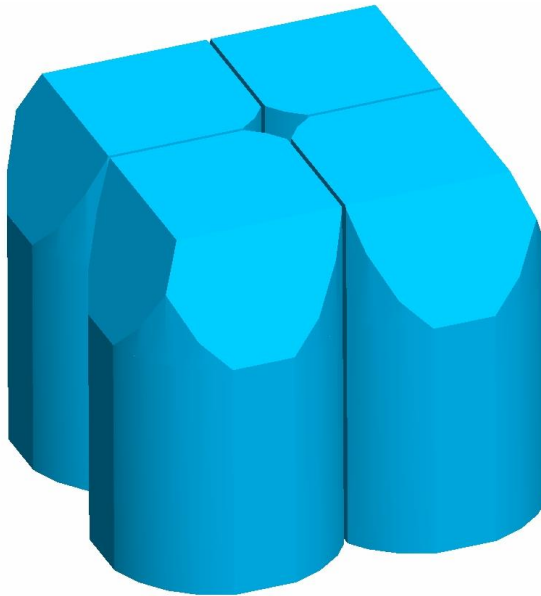


Figure 4.2 – Shape and orientation of the four crystals of an EXOGAM clover detector.

All dimensions of the cryostat, the crystals and the anti-Compton shields are taken from the [EXOGAM] web page. There, several technical drawings are provided. However, they did not contain any information about the position and depth of the hole for the core electrode.

As 8 of the 16 EXOGAM detectors were manufactured by ORTEC and the other 6 by CANBERRA EURYSIS the design of the detectors differs. According to [Gros 05], ORTEC detectors have a core electrode which is “off centered” and 82 mm deep on average, whereas the CANBERRA EURYSIS detectors have a “centered” core electrode of ~ 78 mm depth. Unfortunately, the position was not exactly specified, neither for CANBERRA crystals nor for ORTEC crystals. Furthermore, it was impossible to find out, which of the EXOGAM detectors used for the EXILL array

were from ORTEC and which from CANBERRA EURYSIS.

In the present simulation it is assumed that the core electrode is located at the center of the former cylindric crystal. Other positions of the electrode show no impact on efficiency and the response functions agree within statistical fluctuations. This feature is due to a simplified implementation of the detection process, which is discussed in section 4.4.1. Furthermore, a dead layer of ~ 1 mm (see sec. 4.4.2) at the core electrode is assumed.

The distance from the target to the front side of the detector cryostat is also unknown. In the previously mentioned CAD file a distance of ~ 132 mm is specified, which results in a geometrical overlap of the anti-Compton shields of to adjacent detectors. Geometrically the distance is confined by the dimensions of the anti-Compton shields. This leads to a smallest possible distance of 136 mm. Another value of 138 mm is stated in one of the technical drawings from the [EXOGAM] web page. In the absence of a measured value and because it is most conclusive, the latter value is used for the simulation. This corresponds to a target-to-crystal distance of 145 mm.

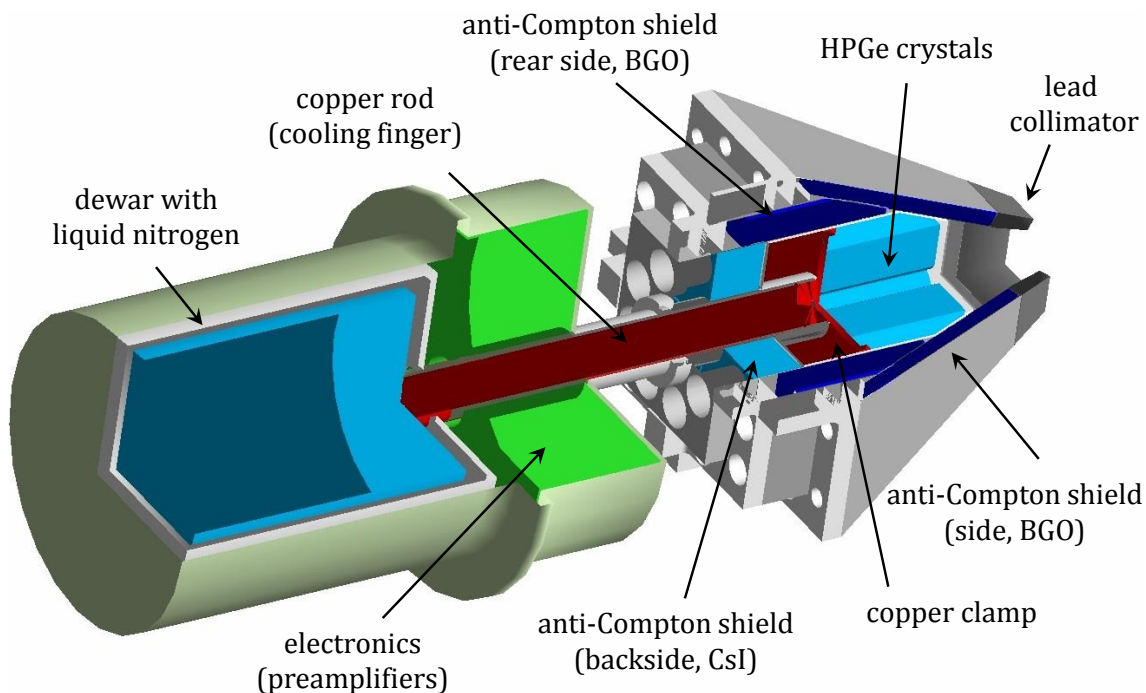


Figure 4.3 – An EXOGAM clover detector with its components.

4.1.2 GASP

The simulation of the GASP detectors is based on a Geant4 geometry provided by [Mene R] and technical drawing from the [GASP] web page. In contrast to the EXOGAM clover detectors, the GASP detectors consist of only one crystal with a cylindrical shape. Its diameter and height are 76 mm and 82 mm, respectively. The front side of the crystals is tapered with an angle of 10° . Together with the preamplifiers and the copper rod (estimated from the technical drawing to ~ 2.5 cm in diameter; it is nowhere exactly specified), the crystal is housed in an aluminum cryostat. To mount the EXOGAM anti-Compton shields on the GASP detectors a special holder was installed, which is also included in the simulation according to the CAD file [Jent M].

The distance from the target to the front side of the cryostat is 124 mm. This value provides the same distance to the target for the anti-Compton shields of all EXOGAM and GASP detectors. The target-to-crystal distance is 130 mm.

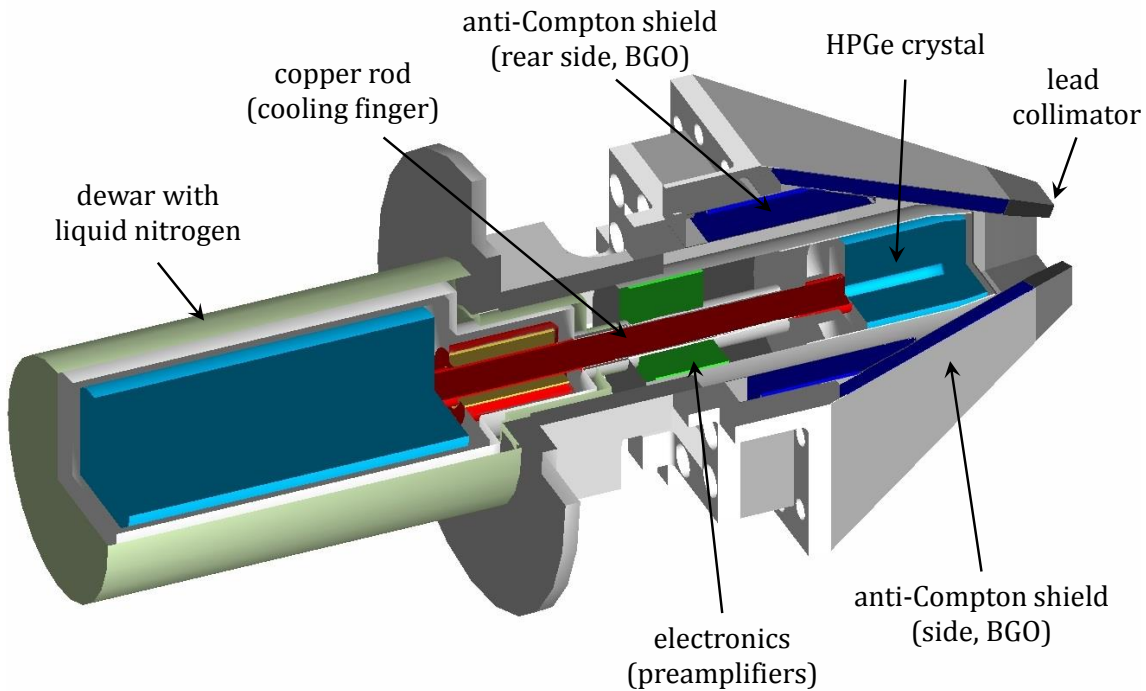


Figure 4.4 – A GASP detector with its components.

4.1.3 LOHENGRIN

Similar to the EXOGAM detectors, the LOHENGRIN detectors are clover detectors housing 4 crystals in one cryostat. The shape and placement of the crystals inside the cryostat is based on values used for a simulation in [Mart 06] (a simulation of the LOHENGRIN detectors with MCNP) and on [Lang H]. However, detailed information about the crystal shape cannot be found, because this information has not been written down while manufacturing.

The crystals are made from a cylindric HPGe crystal, 80 mm in height and 50 mm in diameter.

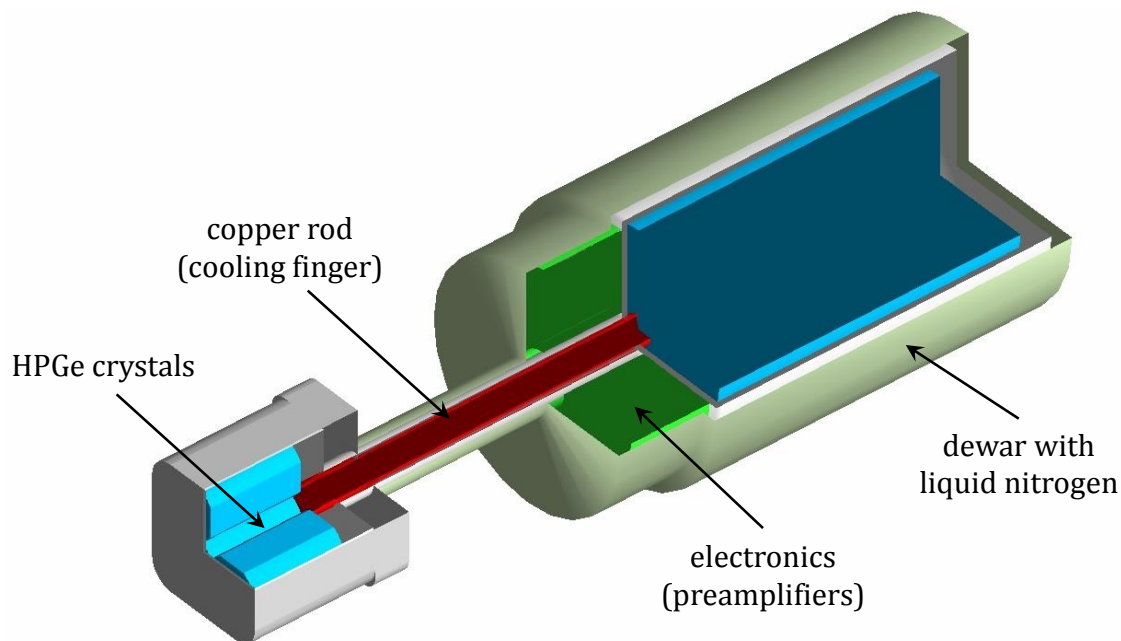


Figure 4.5 – A LOHENGRIN detector with its components.

4.2 Response & Efficiency

In this work the motivation to build a simulation of the EXILL detector array was to determine the detector response. The response matrix shown in figure 4.6 was achieved by simulating the spectra generated by isotropically emitted gamma rays with energies ranging from 5 to 10595 keV in 10 keV steps. For each energy 10^6 events were simulated. To compare the simulation with the ^{152}Eu and $^{35}\text{Cl}(n,\gamma)$ measurements in section 4.3, the response was simulated using a point-like source. When doing the response correction for the $^{77}\text{Se}(n,\gamma)$ data, an extended source was used.

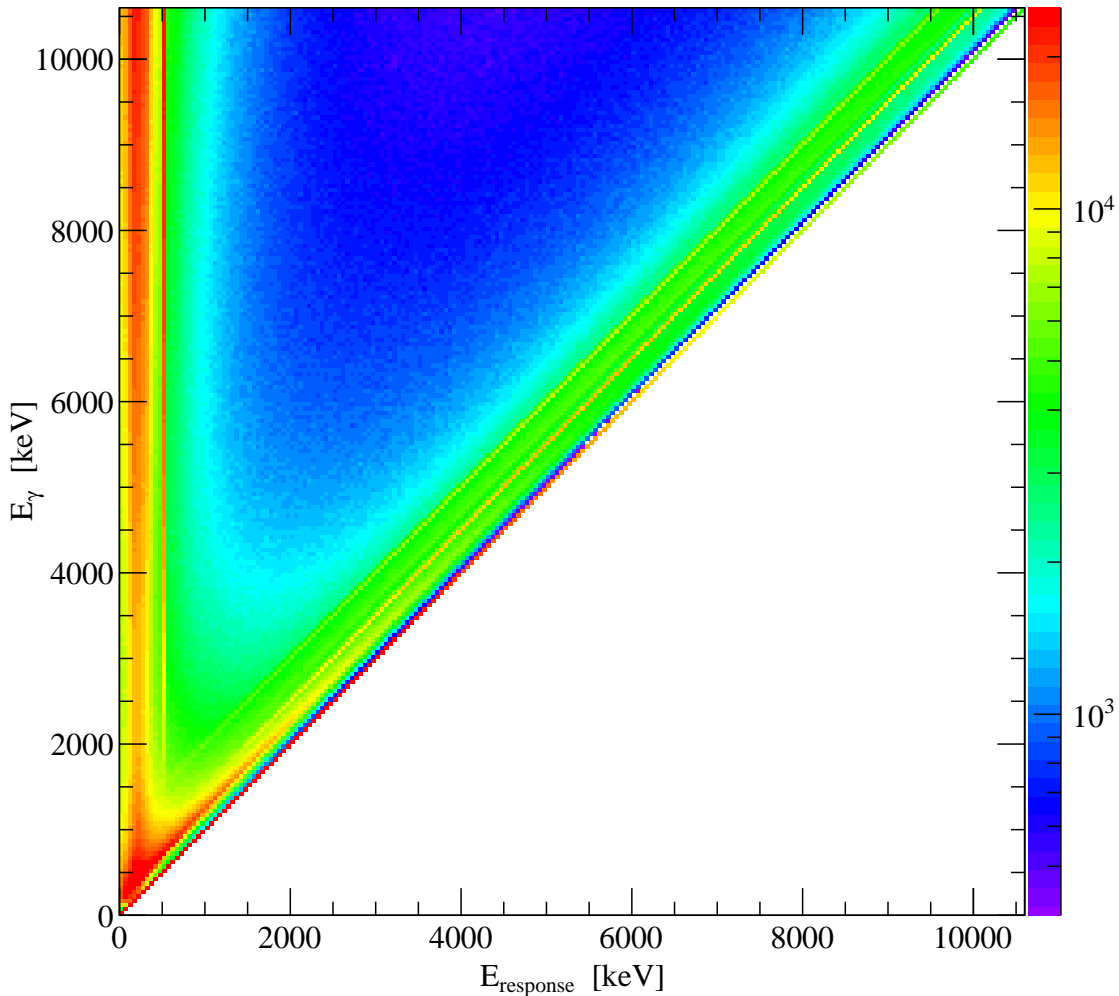


Figure 4.6 – Response matrix of a crystal of the EXOGAM detector 4. The main diagonal is formed by the full-energy peak and parallel to it the escape-peaks are clearly visible. Together with the annihilation peak at 511 keV, they are distinguishable only for gamma-ray energies above ~ 1500 keV. The rest of the response matrix is formed by the Compton-continuum.

A representative outcome of this is presented in figure 4.7. There the response of an EXOGAM crystal for the gamma-ray energies 3 and 10.6 MeV with its statistical uncertainties is presented in red. One can see that the simulated Compton continuum suffers from poor statistics as the relative error in that region is around 20%.

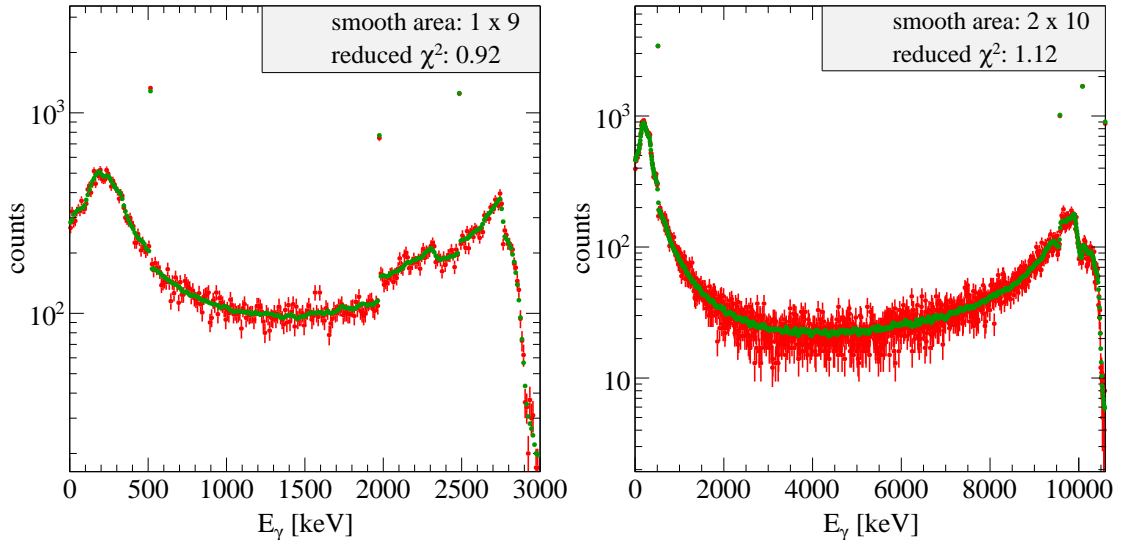


Figure 4.7 – Smoothing of the simulated response functions. After smoothing (green spectrum) the simulated spectrum (red), the uncertainties were reduced to about 3% (as large as the green marks). For high gamma energies a pattern size of 2×10 was used. The algorithm automatically reduces the pattern size for incident gamma rays below 3 MeV to account for quick changes in the response matrix.

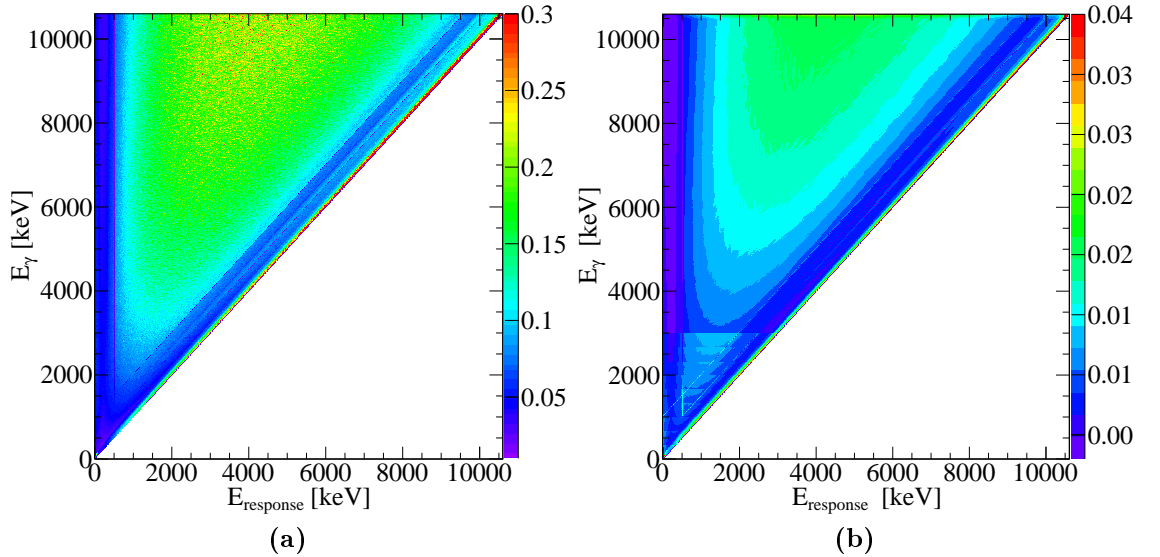


Figure 4.8 – The relative uncertainties of the response matrix before (a) and after (b) smoothing. With the smoothing of the response function, the uncertainties can be reduced significantly. The step-like structure in the smoothed matrix at low energies is due to the decreasing pattern sizes. Hence, the averaging is done with fewer bins and the relative uncertainties are larger. The very high relative uncertainties close to the main diagonal is the gap between full-energy peak and the Compton edge. Note the different scales for the uncertainties!

For the response correction of measured spectra it is important that the Compton continuum is rather smooth. To reduce the fluctuations it would be possible to either simply simulate more events or to smooth the response matrix. The former has the disadvantage that it is very time consuming since one has to simulate 100 times more events to reduce the error to 2%, which takes more than three months with the currently available computing power. It is, obviously, more efficient to smooth the response matrix and depending on the algorithm and its parameters a significant improvement of the fluctuations can be achieved.

The effect of smoothing on the uncertainties of the whole response matrix is visualized in figure 4.8.

In the developed algorithm the new bin content is defined by the average of the bin contents of the current bin and its neighboring bins in the response matrix. The neighboring bins are chosen with respect to the structure of the response matrix around the current bin. As apparent in figure 4.6 the full-energy peaks form the elements of the main diagonal and parallel to it are the escape peaks. In contrast the annihilation peak is constantly at 511 keV.

Therefore, it is convenient to choose the neighboring bins according to a parallelogram-like pattern for bins in the high energy part of the spectra, and according to a rectangular pattern for bins in the low energy part of the spectra (see fig. 4.9).

Furthermore, the response matrix changes quickly for low energy gamma-rays and if the size pattern is too large the smoothed response will differ significantly from the not smoothed response. The algorithm reduces the pattern size automatically at low gamma-ray energies to get consistent results. A χ^2 test of the smoothed spectra shows consistency with the original spectrum and indicates that the slope of the response function did not change during the smoothing.

Apart from the response function the efficiency of the detector can also be estimated with the simulated spectra. This is also used to evaluate the simulation and discussed in more detail in section 4.3.

Similar to equation 2.9, the full-energy efficiency $\varepsilon_{\text{FE, sim}}$ is calculated via equation 4.1 where N_{events} is the number of simulated events during the simulation.

$$\varepsilon_{\text{FE, sim}}(E_\gamma) = \frac{N_{\text{FE, sim}}(E_\gamma)}{N_{\text{events}}} = \frac{N_{\text{FE, sim}}(E_\gamma)}{10^6} \quad (4.1)$$

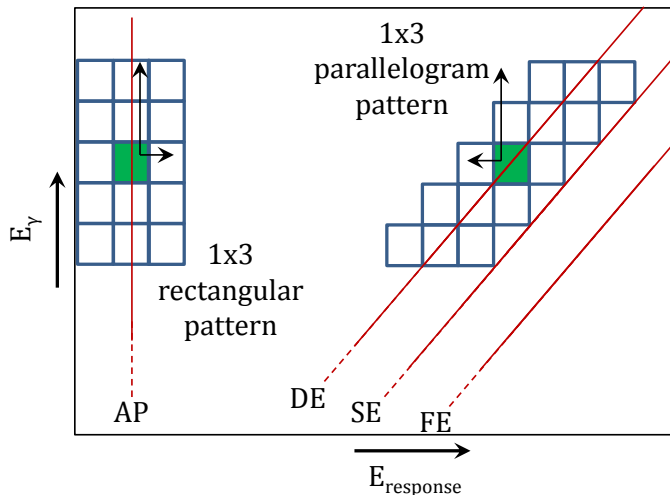


Figure 4.9 – Scheme of the neighboring bins used for smoothing. At high energies in the response spectra, a parallelogram-like pattern is used, following the trend of the full-energy (FE) and escape peaks (SE and DE). At low energies a rectangular pattern is used according to the slope of the annihilation peak (AP).

4.3 Evaluation

To assure the validity of the simulation, the characteristics of simulated spectra have to be compared with measured data. In the following, the efficiencies, escape-to-full-energy peak ratios as well as the spectra of the ^{152}Eu decay and $^{35}\text{Cl}(n,\gamma)^{36}\text{Cl}$ reaction are used to check if simulation and experiment are in reasonable agreement.

Figure 4.10a and 4.10b show the efficiency as a function of the gamma-ray energy and the relative deviation between simulation and experiment, respectively. Hereby, the emphasis is on the slope of the efficiency curve, as the absolute experimental value is not known precisely (this issue is discussed in section 5.1). From figure 4.10b it is evident that the measured data points are well reproduced by the simulation within an uncertainty of $\lesssim 5\%$. Also the interpolated experimental efficiency curve is in line with the simulated one.

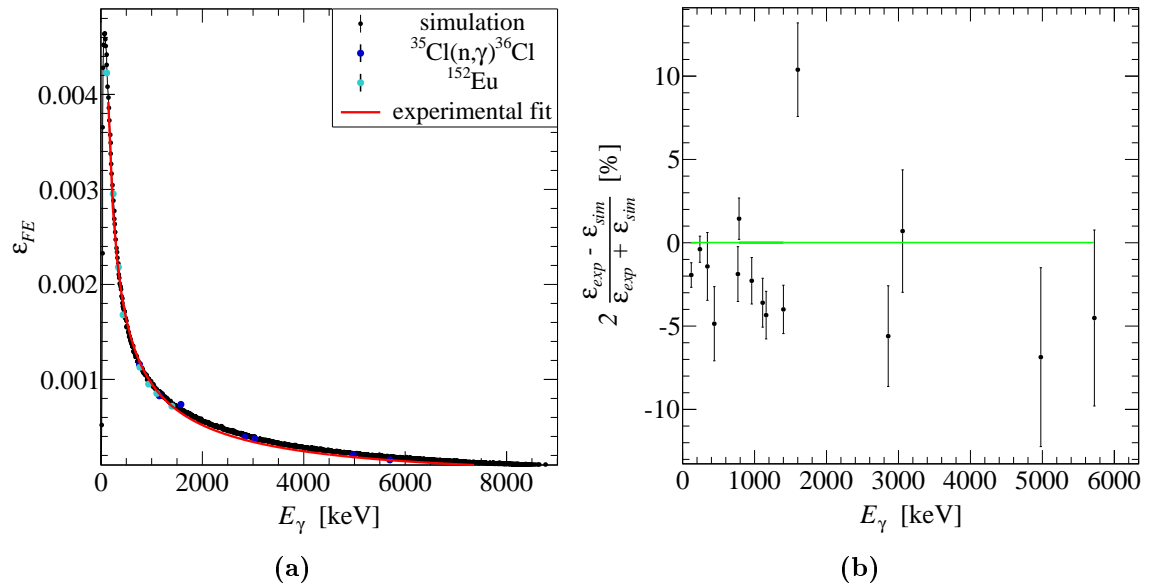


Figure 4.10 – Comparison of simulated and measured efficiency. The experimental data points are calculated assuming an activity of 102 kBq for the ^{152}Eu source (see 5.1). With this assumption, not only the slope but also the absolute value of the simulated efficiency exhibits very good agreement with the experiment.

The comparison of the escape-to-full-energy peak ratios is shown in figure 4.11. For the experimental values, the data from the measured neutron-capture reaction on ^{77}Se and ^{35}Cl were used. The comparatively large errors of the chlorine measurement are due to low statistics. Simulation and experiment agree within the 1σ -uncertainties, which supports the validity of the simulation.

The presented values relate to a single crystal of the EXOGAM detector 4, but they are representative for all detectors.

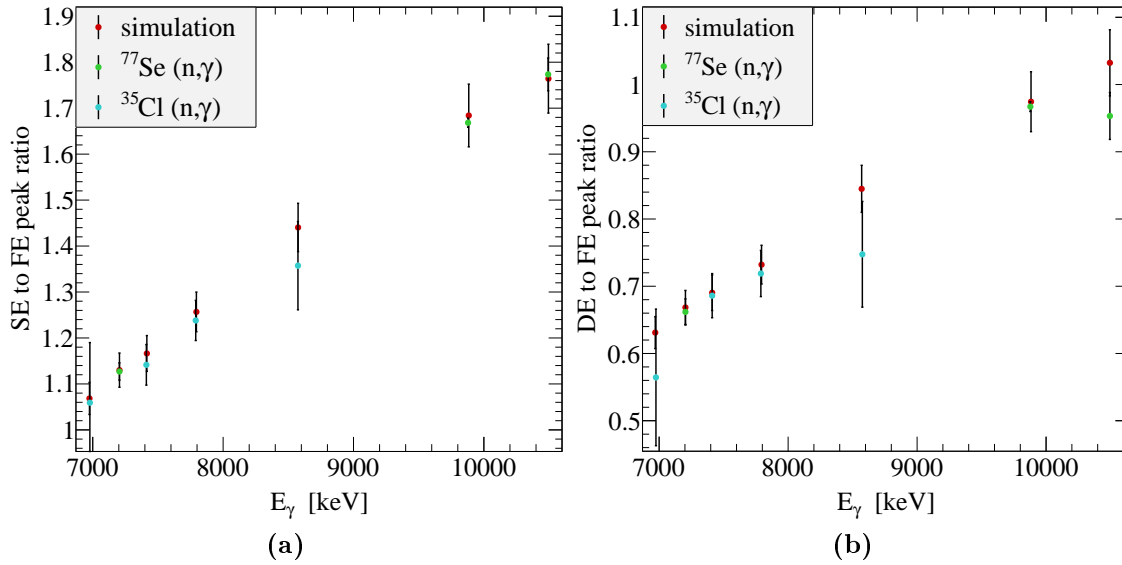


Figure 4.11 – Comparison of the escape-peak to full-energy peak ratios: (a) single-escape peaks, (b) double-escape peaks. The very good agreement indicates, that the geometry of the crystal is well implemented in the simulation.

Very important for the response correction is a good estimation of the Compton continuum. Unfortunately, no measurement with a calibration source such as ^{137}Cs or ^{88}Y with only one or two gamma-ray transitions has been made. Those would have been perfect to directly compare simulated and measured Compton continua. Instead, the simulated response functions have been used to create a ^{152}Eu spectrum (using the branching ratios provided by [ENSDF]), which then is normalized to the measured ^{152}Eu spectrum.

As one can see in figure 4.12, the general shape is very well reproduced. However, an issue is the "perfect resolution" of the simulation (see 4.4.1), as this leads to an overestimation in those bins where there is a peak, and to an underestimation in the bins next to it. Because of the detector resolution in the experiment, the peaks in the measured spectra are spread out over several bins and if the peak mean is close to the border of a bin, this peak is more or less shared between the two neighboring bins.

This effect is also visible if one looks at the relative deviation between the simulated and measured spectrum in figure 4.12b. In the range from 400 to 1200 keV the deviation is less than 5 to 10 % except for the peaks. There the missing detector resolution leads to larger deviations, as it was just explained. Below 100 keV the simulation does not describe the experiment very well, but this region is also not of interest for the further analysis. Above 1200 keV the deviation increases as well, which is because of the missing detector resolution in the simulation, but also because of pile-up effects that are difficult to implement in the simulation and therefore neglected.

Despite these shortcomings, the simulation appears to be a good representation of the real detector assembly, which is also supported by good χ^2 values when comparing the spectra in the range from 400 to 1200 keV. They reach from values around 0.8 to 1.5 for different crystals if smoothed response functions are used. If the response functions are not smoothed, the χ^2 values are worse (around 2), which supports the use of smoothing.

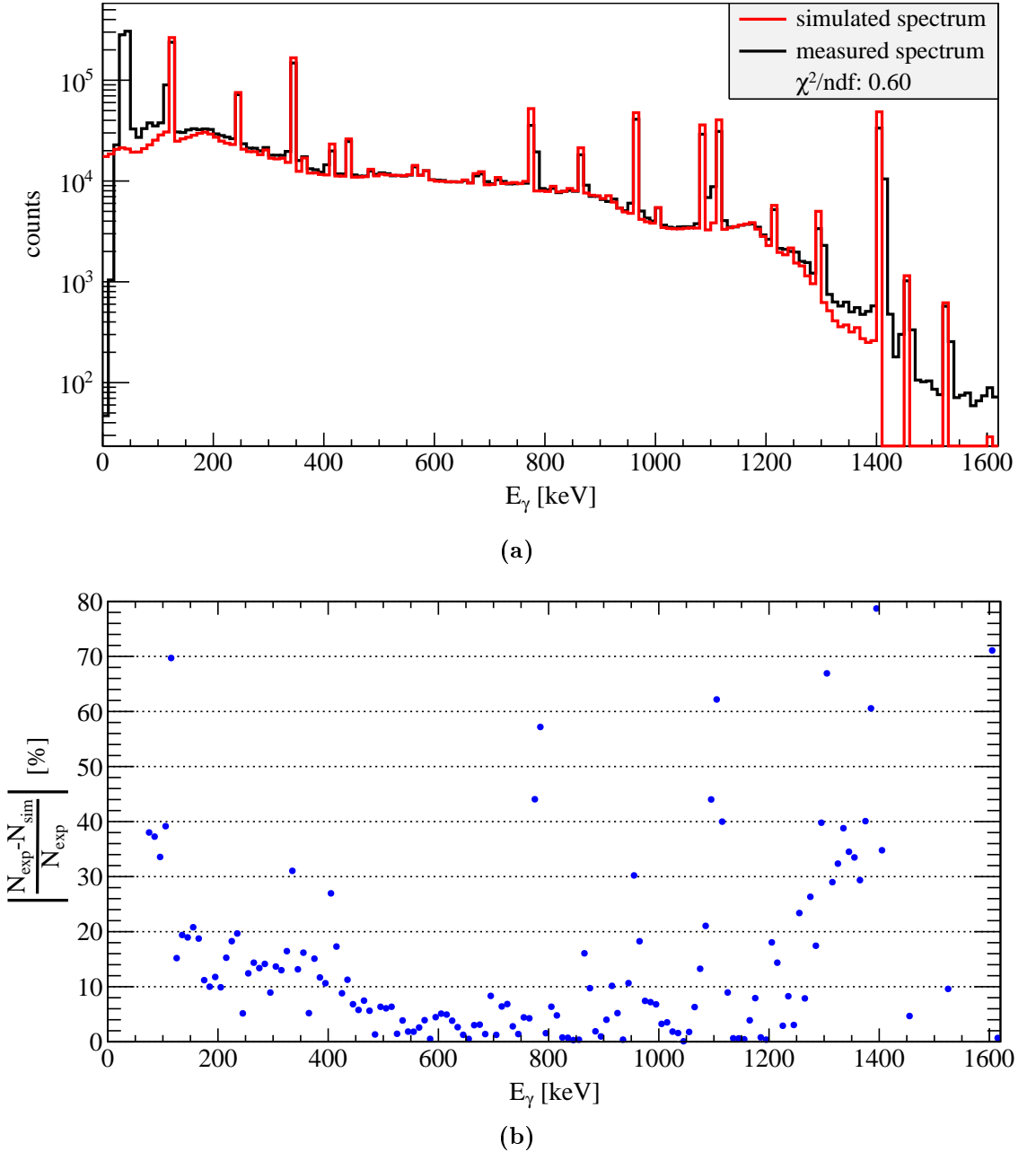


Figure 4.12 – The spectrum of the ^{152}Eu decay generated with the simulated response functions (a) and its comparison with the measured spectra. Figure (b) shows the relative deviation between simulation and experiment, which is further discussed in the text.

The same as for the ^{152}Eu spectrum applies for the $^{35}\text{Cl}(n,\gamma)^{36}\text{Cl}$ spectrum (see figure 4.13). However, it has to be emphasized, that with more than 400 known gamma-ray transitions, the latter is a much more complicated spectrum than the one of the ^{152}Eu decay. Due to the large number of significant peaks and the not implemented detector resolution, there are many individual bins where the relative deviation (see figure 4.13b) is comparatively high. But a closer look reveals, that for the majority of the bins the relative deviation is less than 10 or even less than 5%. This means that the Compton continuum is well estimated by the simulation.

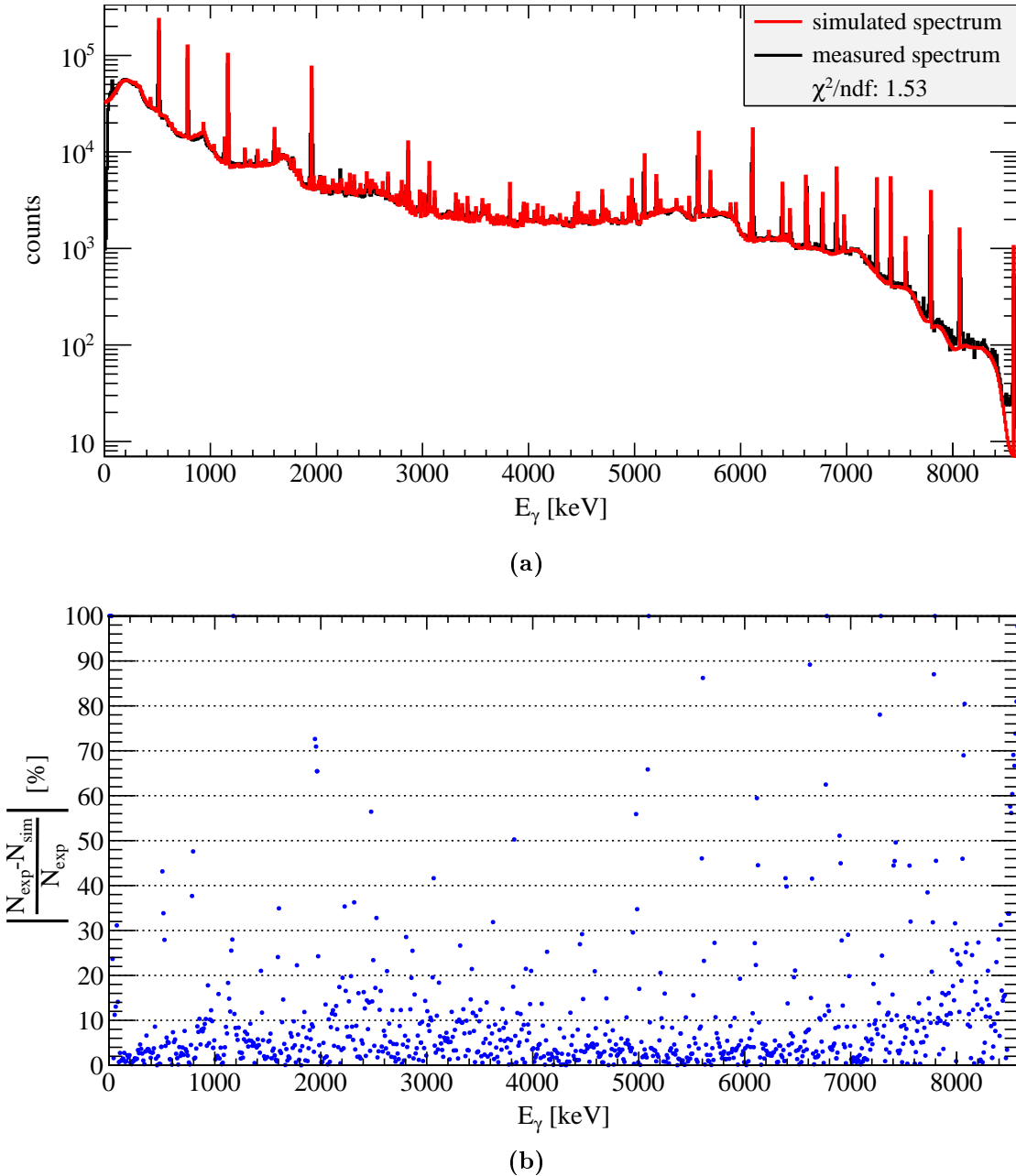


Figure 4.13 – The spectrum of the $^{35}\text{Cl}(n,\gamma)^{36}\text{Cl}$ reaction generated with the simulated response functions (a) and its comparison with the measured spectra. Figure (b) shows the relative deviation between simulation and experiment, which is further discussed in the text.

4.4 Discussion

All in all, the simulation delivers reasonable estimations for the detector response, as far as it is possible to crosscheck that with the experiment. The problems and shortcomings of the simulation, their impact on the analysis and how they could be corrected, if needed, are explained in this section.

4.4.1 Detector Resolution

In a real detector the position of the core electrode influences the electric field in the crystal and therefore the process of charge collection. This, of course, affects the response function. In the simulation the electric field and the production of charge carriers is neglected. Instead, the energy that the incident gamma ray loses directly during the interaction process in the crystal is taken as the measured value. An implementation of the electric field is restricted for several reasons:

- The electric field throughout the crystal is not precisely known. A calculation is, due to the non-trivial crystal shape, a tedious task. One may be able to get a first idea of the electric field from [Gros 05].
- Such a complex and inhomogeneous field is very difficult to implement in Geant4.
- If the electric field is implemented, the simulation of the production of the electromagnetic shower, the drift of the charge carriers in the electric field and their detection at the electrodes is a very time consuming computational task.

All together the gain in accuracy does not justify the much more intensive computer calculations and the effort needed to implement the electric field and the processes of charge production and collection. Neglecting these processes results in the effect that simulated detector response is primarily determined by the position, orientation, outer shape and active volume of the crystal. Hence, the position of the inner electrode does have less impact on the response function than the depth of the electrode and the width of the dead layer, which both affect the active detector volume.

A consequence of this simplification is that the peaks in the simulated spectra are not broadened. However, if needed, one can fold the simulated detector response with measured detector resolutions to obtain a detector response with the proper peak shape. This has not been done yet as the peak shapes and resolutions are very different from crystal to crystal in the EXILL array. Furthermore, it makes the procedure for the response correction more complicated if not impossible. In addition to this, a larger bin width in the spectra compensates to some extent the lack of a proper implementation of the detector resolution.

4.4.2 Dead Layer

In HPGe detectors the contacts for the high voltage are usually made by lithium diffusion (n^+) and boron implantation (p^+). The charge carriers produced in these regions are not fully collected, therefore they represent dead layers [Knol 10]. Whereas the p^+ contact is just a few tenth of micrometers thick and therefore negligible, the lithium drifted n^+ contact is hundreds of micrometers thick. The latter reduces the active volume significantly, which affects the detector response, in particular the efficiency. Its initial thickness depends on the manufacturing process but if the detector is not cooled for a longer period of time, the lithium can slowly diffuse further into the crystal. Hence, the exact dead-layer thickness is unknown especially since all the detectors participating in EXILL are older than 10 years and perhaps have been warmed up during the transport from one experiment to another several times. Depending on whether the n^+ or the p^+ contact is the central contact, HPGe detectors are classified as n-type or p-type detectors, respectively.

In [Huy 10] the effect of a growing dead layer was studied with a p-type HPGe-detector. There it has been shown that the decreasing efficiency of the investigated detector is due to a thicker dead layer, which grew ~ 1 mm during 13 years of operation. Although all detectors used for EXILL are n-type detectors, the process of lithium diffusion is the same and the active volume gets smaller as the detector gets older. Because most of the used detectors are older than 10 years, a dead layer of 1 mm is reasonable and as it is shown in 4.11, it leads to consistent results.

That the dead layer width has a crucial influence on the detector response can be seen for example at the overestimated escape-to-full-energy peak ratios in figure 4.14, where a 2 mm thick dead layer is assumed. In particular the double-escape peaks are overestimated.

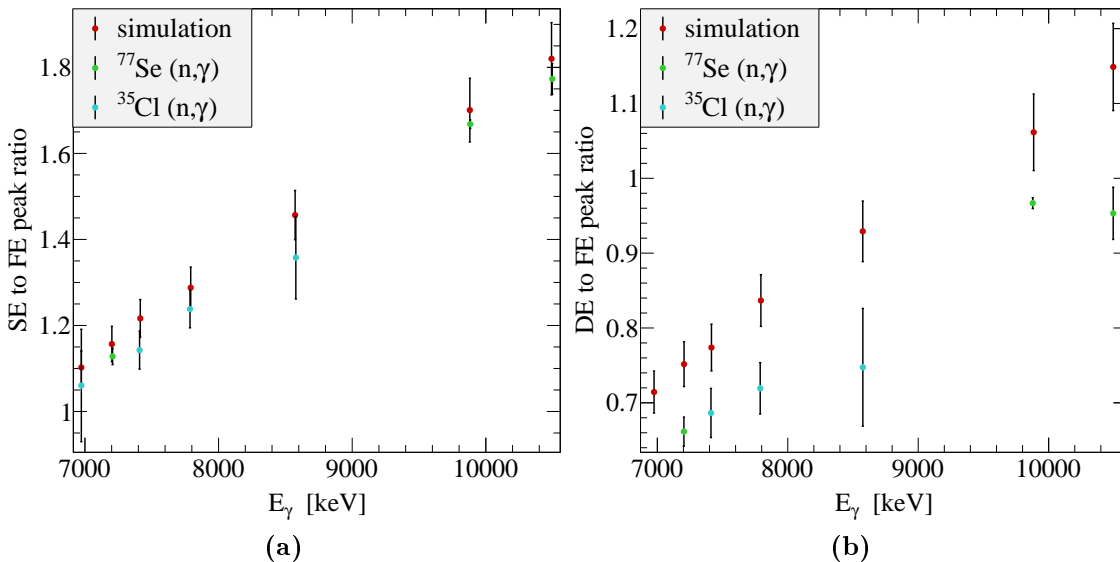


Figure 4.14 – Comparison of the escape-peak to full-energy peak ratios with a dead-layer width of 2 mm: (a) single-escape peaks, (b) double-escape peaks. In contrast to a 1 mm thick dead layer (fig. 4.11) the ratios are overestimated.

Together with the target-to-detector distance and the depth of the hole for the core contact (see sec. 4.1.1), the dead-layer width is an unknown parameter which certainly has a significant impact on the detector response. As these parameters are also different for each detector and crystal, there are in total 72 free parameters for the EXOGAM detectors.

The simulation in its current state has only one geometrical description for the EXOGAM, GASP and LOHENGRIN detectors, respectively. The dead layer width of 1 mm and the target-to-detector distances which are currently implemented in the simulation results in good agreement with experiment for the most of the 46 individual crystals. But for some crystals it is desirable to improve their implementation.

In order to describe each crystal individually, the simulation code needs a major modification and the free parameters must be determined. At the moment, extensive simulations with different trial parameters are running to achieve the latter. By comparing the experimental data with the results of simulations done with different parameters combinations, the best fit can be used as an estimation of each crystal's parameters. This analysis and the overhaul of the simulation code is going to be part of the future work.

5 Analysis

Besides the EXILL detector simulation, a goal of this work was the investigation of the quasi-continuum of coincidence spectra and to see whether it is possible to deduce new aspects concerning the Axel-Brink hypothesis (see section 2.3.1). According to this hypothesis, the strength function depends only on the gamma-ray energy and the multipole type of the emitted gamma radiation. Hence, the idea was to create coincidence spectra gated on low-lying excited states and compare their strength functions. If they would appear to be the same, it would be a hint that the hypothesis is actually true.

The treatment of the raw data until the desired spectra are generated can be divided into the following steps which are explained in more detail in the sections 5.1 to 5.4:

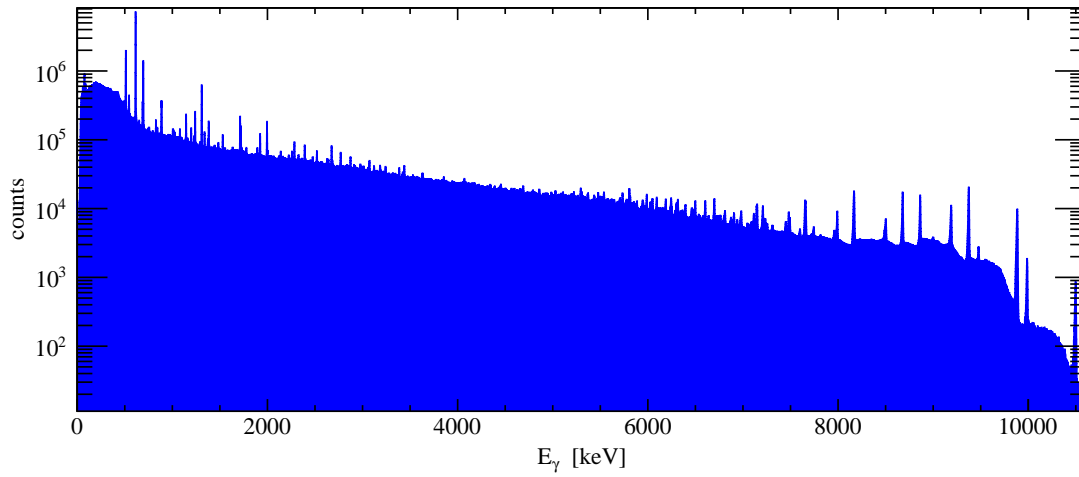
- energy calibration of the raw data
- determination of the efficiencies for all detectors/crystals
- generation of coincidence spectra
- applying the response correction with response functions derived from the simulation
- applying the efficiency correction
- deduction of strength functions with the help of a statistical gamma-cascade simulation code

The energy calibration has been done by [John 14]. In the same work a script was also developed to store the raw data in form of a *TTree*, which is a list-mode data-format used within the [ROOT] framework. Based on these energy calibrated data sets, the whole analysis was done using the aforementioned framework.

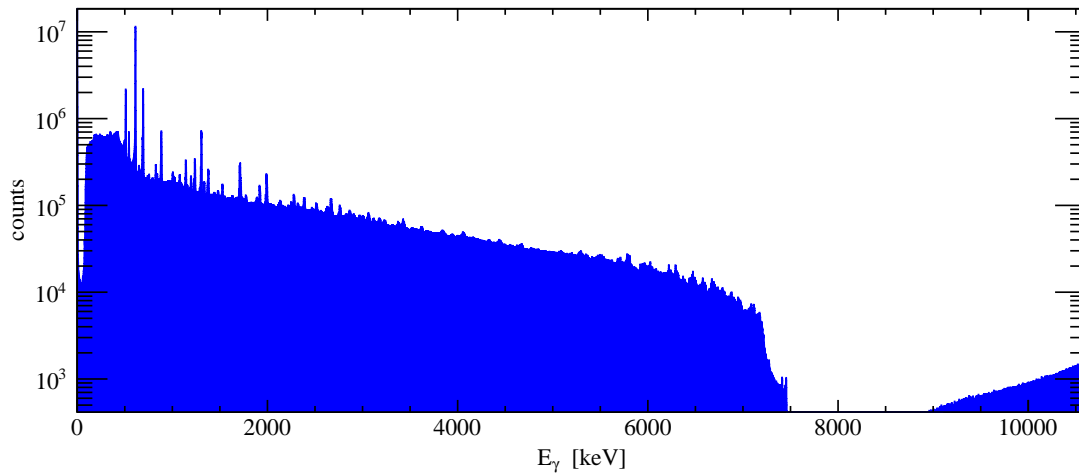
During the creation of the coincidence spectra a problem occurred, which hindered the further analysis, namely the response correction. This is discussed within section 5.3.

It should be emphasized again that all steps discussed in this section have only been performed for the crystals of the EXOGAM detectors. In figures 5.1a to 5.1c examples of spectra from the three different types of detectors are presented. Above 7 MeV the GASP and LOHENGRIN detectors contain no information, probably because of incorrectly tuned amplifiers.

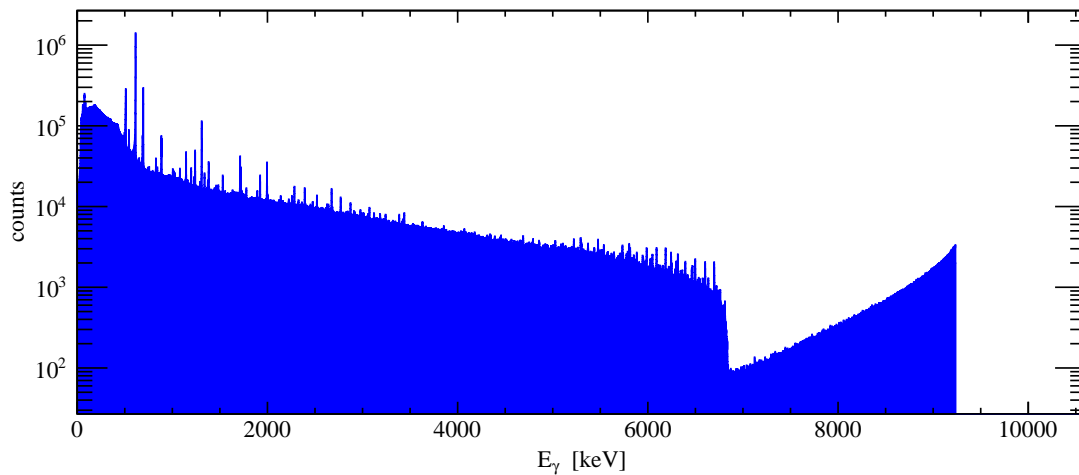
For the determination of the efficiencies and in order to define energy-gates for the coincidence spectra, the peaks of the measured spectra must be approximated by a proper fit function. Furthermore, the presence of clover detectors potentially enables the use of add-back. Both aspects are the subject of the following two paragraphs.



(a) EXOGAM



(b) GASP



(c) LOHENGRIN

Figure 5.1 – Examples of the spectra measured with the EXOGAM (a), GASP (b) and LOHENGRIN (c) detectors. The EXOGAM detectors measured the full spectrum of the $^{77}\text{Se}(n,\gamma)^{78}\text{Se}$ reaction, whereas the GASP and LOHENGRIN detectors did not work for energies above 7 MeV.

Add-back correction

Since the majority of the used detectors were clover detectors comprising four individual crystals, it is possible to apply the so-called “add-back”. The idea is, that incident photons that interacted with a crystal via Compton scattering or pair production and did not deposit all their energy in one crystal, might deposit the rest of the energy in a neighboring crystal of the same clover detector. This is then detected as if there were two separate events, although there was only one incident photon. By applying a time condition (usually in the order of 10 to some 100 ns) one can filter and add up those events, hence restore the information about the energy of the incident photon. This method leads to a reduction of the Compton continuum and to an enhanced efficiency. However, for the analysis of discrete and resolved peaks add-back is a convenient method, but by applying this method, one has to use the response function of the whole clover detector (which depends on the time window that is used to do add-back) instead of the response function of a single crystal. Obviously the composition of the response function becomes more complex, hence its simulation is an even more challenging task. For that reason the response correction is always applied on spectra without add-back.

However, in order to test the event-builder which is explained in section 5.3, some add-back spectra were created and compared with the spectra where no add-back was applied. An example is shown in figure 5.2. There the difference of a spectrum with and without add-back is presented. It is clearly visible that the number of low energy gammas is less in the spectrum with applied add-back, in favor of an improved yield in the peaks. Furthermore, the yield of the annihilation peak together with those of the escape peaks is significantly reduced and added up to the corresponding full energy peak.

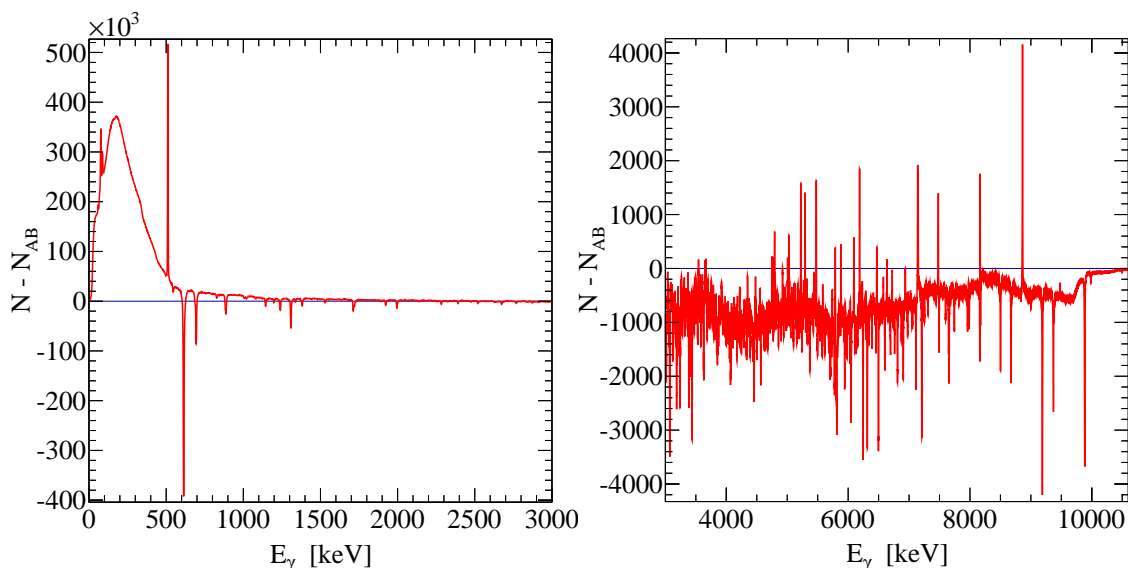


Figure 5.2 – A comparison between a spectrum with and without applied add-back. The red line is the difference of these two spectra. Negative values mean an improved yield after the add-back is applied.

Fit function – TkT

As already stated in previous chapters different crystals exhibit very different peak shapes. In section 2.4 it was already explained why peaks of spectra that were measured with HPGe detectors might have a left tail, but as it is obvious from figure 5.3 some peaks have a right tail or even exhibit tails on both sides.

The tail on the right side could come about due to a not properly calibrated baseline in the digitizers. This could then lead to an overestimation during the integration of the measured electric pulse, hence to a tail on the right side.

In order to get proper fits of those peaks, it is necessary to not only fit with Gaussian, but also with a function that accounts for the tails on both sides. The interactive tool “TkT” [Bazz D], which is used in the AGATA collaboration for their analysis, provides such a fit-function. It also includes a background estimation with an additional step function and linear function. Furthermore, it supports the fit of several peaks in case they are very close to each other.

After fitting a peak, TkT prints the values of all fit parameters as well as the peak area, its errors and the value of the reduced χ^2 . The fit function f_P is constructed as follows:

$$f_P = A(f_G + f_{LT} + f_{RT} + f_S) + B_0 + xB_1 \quad (5.1)$$

It comprises a Gaussian f_G , a left tail f_{LT} , a right tail f_{RT} and a step function f_S :

$$f_{LT}(x; P, \sigma, l) = e^{\frac{l^2 + 2l(x-P)}{2\sigma^2}} \quad x \leq P - l \quad (5.2)$$

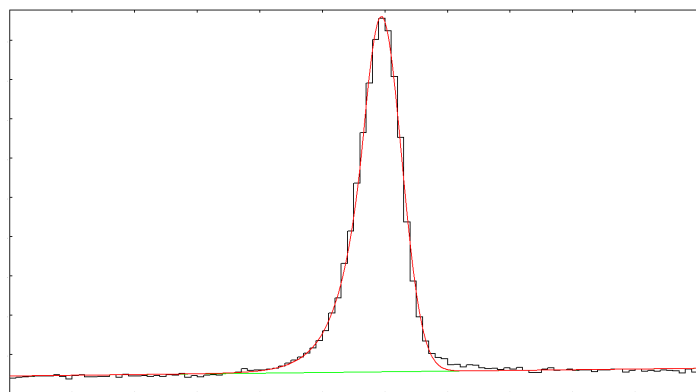
$$f_G(x; P, \sigma) = e^{-\frac{(x-P)^2}{2\sigma^2}} \quad P - l \leq x \leq P + r \quad (5.3)$$

$$f_{RT}(x; P, \sigma, r) = e^{-\frac{r^2 + 2r(x-P)}{2\sigma^2}} \quad x \geq P + r \quad (5.4)$$

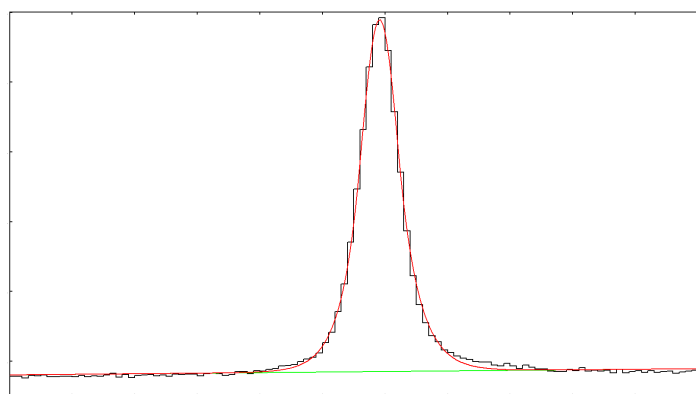
$$f_S(x; P, \sigma, S) = S(1 + e^{\frac{x-P}{\sigma}})^{-2} \quad (5.5)$$

The function depends on 8 parameters which are:

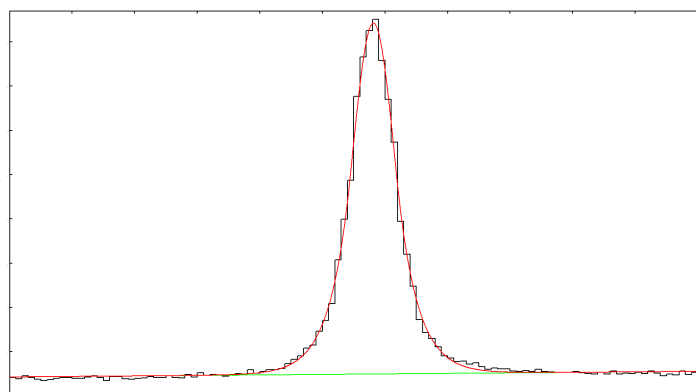
- A : peak amplitude
- P : peak position
- σ : peak width
- r : distance from P to the beginning of the right tail
- l : distance from P to the beginning of the left tail
- S : amplitude of the step
- B_0 : constant
- B_1 : slope of the linear background function



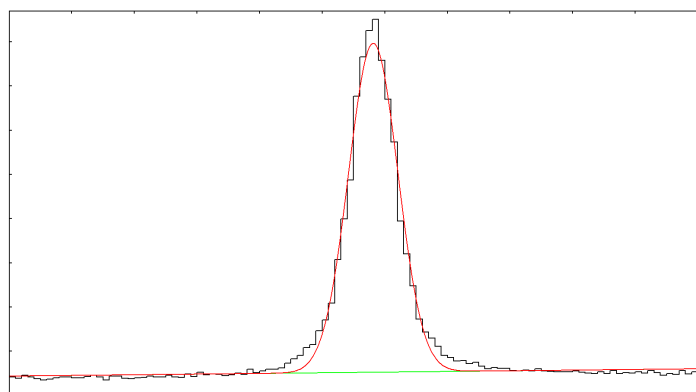
(a) left tail



(b) right tail



(c) both tails



(d) both tails – fit with Gaussian

Figure 5.3 – Peak shapes fitted with TkT

5.1 Detector Efficiency

In order to evaluate the quality of the detector simulation which is presented in section 4, the absolute efficiency is a good experimental quantity for that purpose. Furthermore, it can be used to correct the measured spectra and to calculate other absolute quantities. In section 5.4 the efficiency corrected spectra are compared with the simulation of γ Dex to get information about strength functions.

^{152}Eu decay		$^{35}\text{Cl}(n,\gamma)^{36}\text{Cl}$	
peak energies [keV]	I [%]	peak energies [keV]	I [%]
121.78	28.53	786.30	} 26.61
244.70	7.55	788.42	
344.28	26.59	1131.24	
443.96	} 3.13	1327.40	1.88
444.01		1601.07	1.21
778.90	12.93	2676.32	3.65
963.37	} 14.65	2863.81	} 6.05
964.06		2866.88	
1109.18	} 13.86	4979.89	3.71
1112.08		5715.36	5.47
1408.01	20.87	6977.95	2.23
		7414.09	9.90
		7790.45	8.01
		8578.70	2.66

Table 5.1 – The energies and relative intensities I of the transition used for the efficiency calculation. The intensities are given per 100 decays and 100 captures, respectively. As the detector resolution of the EXILL detectors ranging from ~ 3 to ~ 7 keV, the relative intensities of transitions close to the used strong transitions were added up.

For the present work, measurements of the ^{152}Eu decay and the $^{35}\text{Cl}(n,\gamma)^{36}\text{Cl}$ reaction have been used to determine the absolute efficiency of the EXILL setup.

The analyzed transitions and their relative intensities [ENSDF] are listed in table 5.1. They have been chosen in such a way, that the corresponding peaks in the spectra are rather easy to fit, hence some strong transitions have not been used because other peaks were too close and did not allow a good estimation of the background. The relative intensities of weaker transitions that are a few keV next to the analyzed strong transitions are also taken into account (see table 5.1), as the detector resolution is about 3 to 7 keV.

By approximating the peaks with equation (5.1) and calculating their areas, the efficiencies for the corresponding energies have been calculated according to equation (2.9). In contrast to the measurement with the ^{152}Eu source, which had a certain activity (see explanations in the text further below), there is no activity for the $^{35}\text{Cl}(n,\gamma)$ measurement, since there has been no measurement of the neutron flux. Therefore, its peak areas have been divided by the relative intensities

only, resulting in a relative efficiency. Subsequently the obtained relative efficiency has been normalized to the absolute efficiency obtained from the ^{152}Eu measurement.

The energy dependence of the efficiency is approximated with:

$$\varepsilon_{FE}(E_\gamma) = AE_\gamma^b \cdot e^{cE_\gamma} \quad (5.6)$$

An efficiency calculation was already done in a previous work [John 14], but during an overhaul of the utilized code some bugs have been encountered. Nevertheless, the results of the mentioned work were not affected, since the only relevant dependency was that on the slope of the efficiency, rather than a correct absolute efficiency. Unfortunately, in the course of recalculating the efficiencies it turned out that the activity of the used ^{152}Eu source, which was reported in the logbook of the EXILL campaign, is not correct. Namely the value of 70 kBq stated there led to very pronounced discrepancies between the experimentally calculated efficiencies and those which are predicted by the simulation.

There have been only two ^{152}Eu sources at Grenoble that fall into consideration: one with an activity of ~ 102 kBq and another one with ~ 416 kBq [Kost U]. A comparison of the simulated and the measured efficiency based on the former activity was already shown in section 4.3 in figure 4.10. Although the simulated efficiency seems to be slightly above the measured one, they do agree within 5 %.

Furthermore, by extrapolating the efficiency of all the EXOGAM detectors to the efficiency of 16 EXOGAM detectors, the efficiencies of the EXILL and the EXOGAM array at GANIL [EXOGAM] can be compared. The calculated values are presented in table 5.2 and show a good agreement. The uncertainties of the efficiencies obtained from the EXILL array are about 8 % and of statistical nature.

	EXILL array	EXOGAM at EXILL (extrapolated)	EXOGAM (simulated)	EXOGAM (experiment)
622 keV	0.11	0.16	0.17	0.13 - 0.15
1300 keV	0.08	0.11	0.12	0.10

Table 5.2 – Array efficiencies for EXILL and EXOGAM. The efficiency of the EXOGAM detectors were extrapolated from 8 to 16 detectors to compare it with the efficiency of the EXOGAM array at GANIL (simulation and experiment). Within the uncertainty of 8 % for the EXILL efficiencies, these values are consistent.

The fact, that the EXILL simulation and the comparison with the former EXOGAM array are consistent with the experimentally calculated values, points out that simulation itself and the deduction of the efficiencies is trustworthy. Similarly, other groups of the EXILL collaboration performed measurements with a ^{60}Co source of unknown activity. Again there are two different ^{60}Co sources that fall into consideration. As it can be assumed that the detector efficiency has been rather constant

during the whole EXILL campaign, both the ^{60}Co and ^{152}Eu measurements should result in the same efficiency. Out of the four possible combinations of the two ^{152}Eu and the two ^{60}Co sources there is only one where these two efficiencies do agree: 21 kBq for ^{60}Co and 416 kBq for ^{152}Eu . This heavily contradicts the aforementioned consistent results, where a source of 102 kBq is assumed.

This topic is still under discussion within the EXILL community. So far, no absolute efficiencies have been calculated by other members of the community. For the scope of this work, a 102 kBq ^{152}Eu source is used, since it is in favor of the presented results.

5.2 Response Correction

To analyze the quasi-continuum, it has to be separated from the Compton continuum, which is a consequence of the detector response. Therefore, a response correction is inevitable. The way to deduce the response matrix has been described in 4.2. In this section the used algorithm for the correction of the detector response is discussed.

The effect that the detector distorts the spectrum $h(E)$ emitted from a source or the target can be formulated mathematically:

$$h'(E_j) = R(E_i, E_j) \cdot h(E_i) \quad (5.7)$$

The best way to restore the full information about $h(E)$ would be to multiply the measured spectrum $h'(E)$ with the inverse response matrix R^{-1} . Unfortunately, this can only be achieved numerically and since response matrices are usually very large (in this work 1060×1060 !), the inversion is a very time consuming task, if not even impossible. Therefore, other methods have been developed.

The algorithm used herein is called the spectrum strip method. It is the favorable method concerning uncertainties and computing time as a study in [Mass 14] shows. This method follows a comparably easy pattern:

Starting from the top of the spectrum, for each bin the corresponding response function is normalized according to its full-energy peak and then subtracted (except for the full energy peak). One iteration step k can be written as:

$$h^{k+1}(E_i) = h^k(E_i) - R(E_{n-k}, E_i) \cdot r_k \quad i < n - k \quad (5.8)$$

$$r_k = \frac{h^k(E_{n-k})}{R(E_{n-k}, E_{n-k})} \quad r_k \geq 0 \quad (5.9)$$

where n is the number of bins in the spectrum (E_1 is the first bin, E_n the last) and r_k the normalization factor of the k 'th response function. The first iteration $k = 0$ starts with $h^0 = h'$. If the bin content of $h^k(E_{n-k})$ is negative, which can happen due to fluctuations or a slight overestimation in the simulated response function, the normalization factor r_k is set to zero.

As the algorithm starts from the top of the spectrum, it cannot be applied to the spectra measured with GASP or LOHENGRIN detectors as they contain no information above 7 MeV. When applied to a spectrum measured with an EXOGAM detector, the result of the response correction is shown in figure 5.5. There the number of counts per bin has been reduced by one order of magnitude. At high energies (fig. 5.6) one can observe that single and double-escape peaks as well as the Compton continua of the different peaks have been well subtracted, whereas the full-energy peaks remain.

The propagation of uncertainties during the response correction is analytically not feasible, because correlations between different iterations are unknown. It is easily comprehensible that, if at an early iteration step too much detector response is subtracted, the resulting spectrum has too few counts. In turn, too few detector response is subtracted in the following iterations, which compensates to some extent that too much was subtracted before. Therefore, it is obvious that correlations exist.

In figure 5.4 a comparison between an analytical error propagation without correlations and the method described in the text below is shown. Apparently an error propagation without taking into account correlations heavily overestimates the uncertainties.

The uncertainties involved are the statistical fluctuations which are present in the measured spectrum as well as in the simulated response function.

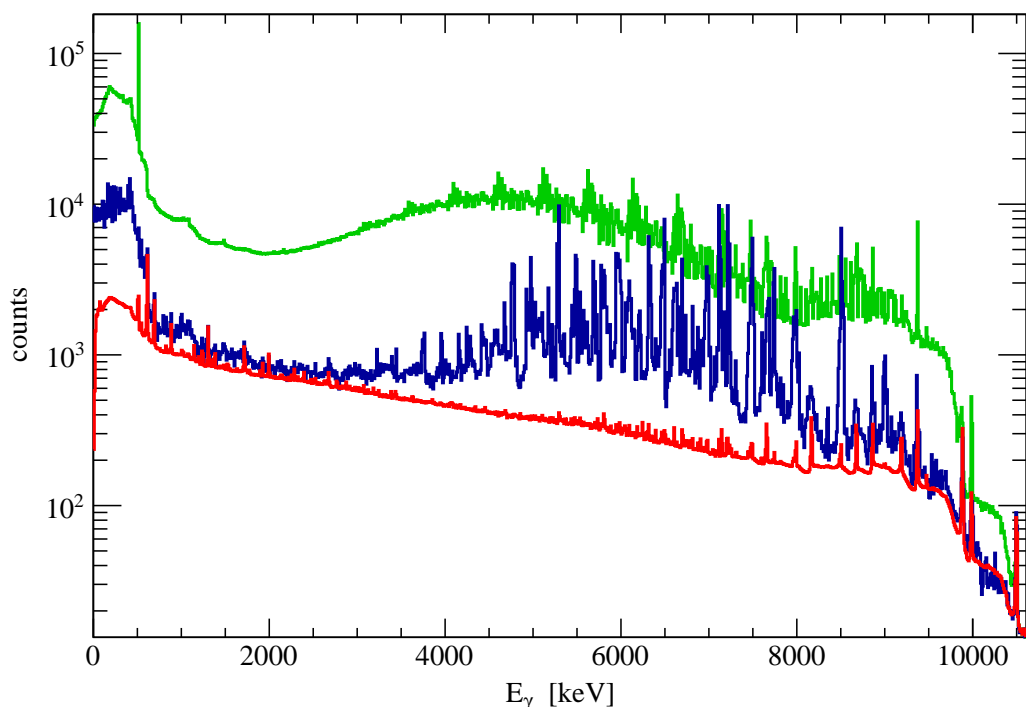


Figure 5.4 – An analytical error estimation without correlations (green) and the numerical error estimation (blue) as described in the text. An analytical error propagation overestimates the uncertainties by an order of magnitude. The statistical uncertainty of the original spectrum is shown in red.

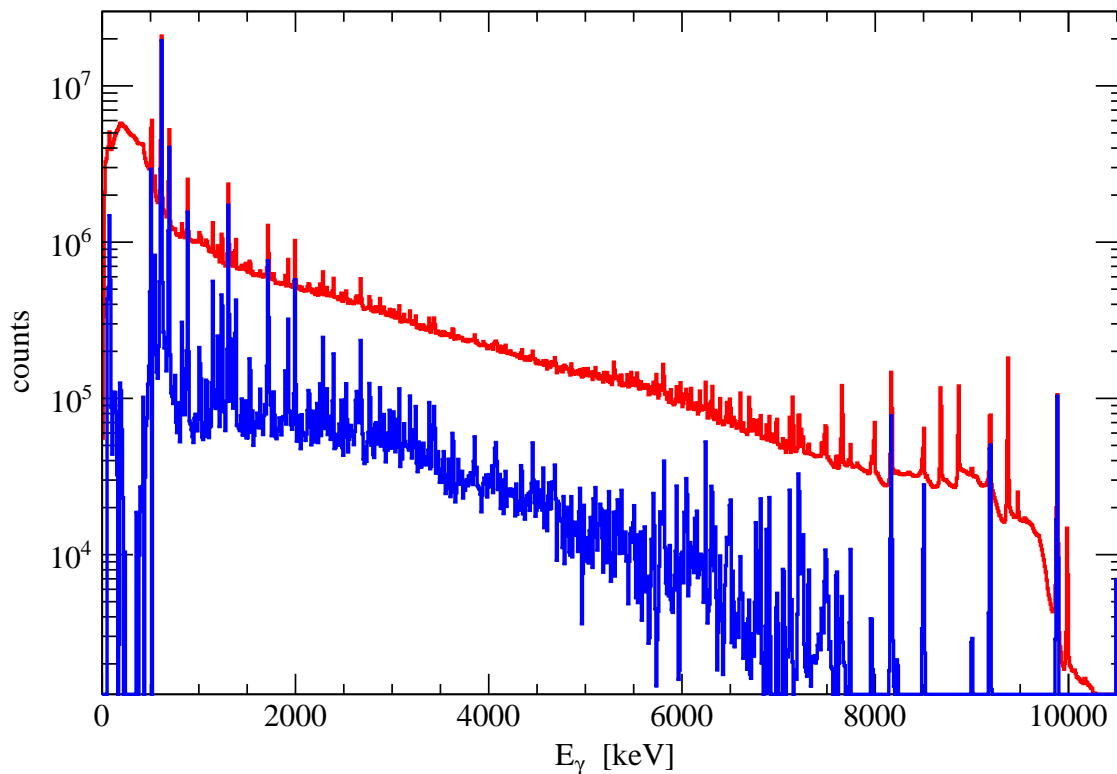


Figure 5.5 – The measured (red) and response corrected (blue) spectrum of the $^{77}\text{Se}(n,\gamma)^{78}\text{Se}$ reaction.

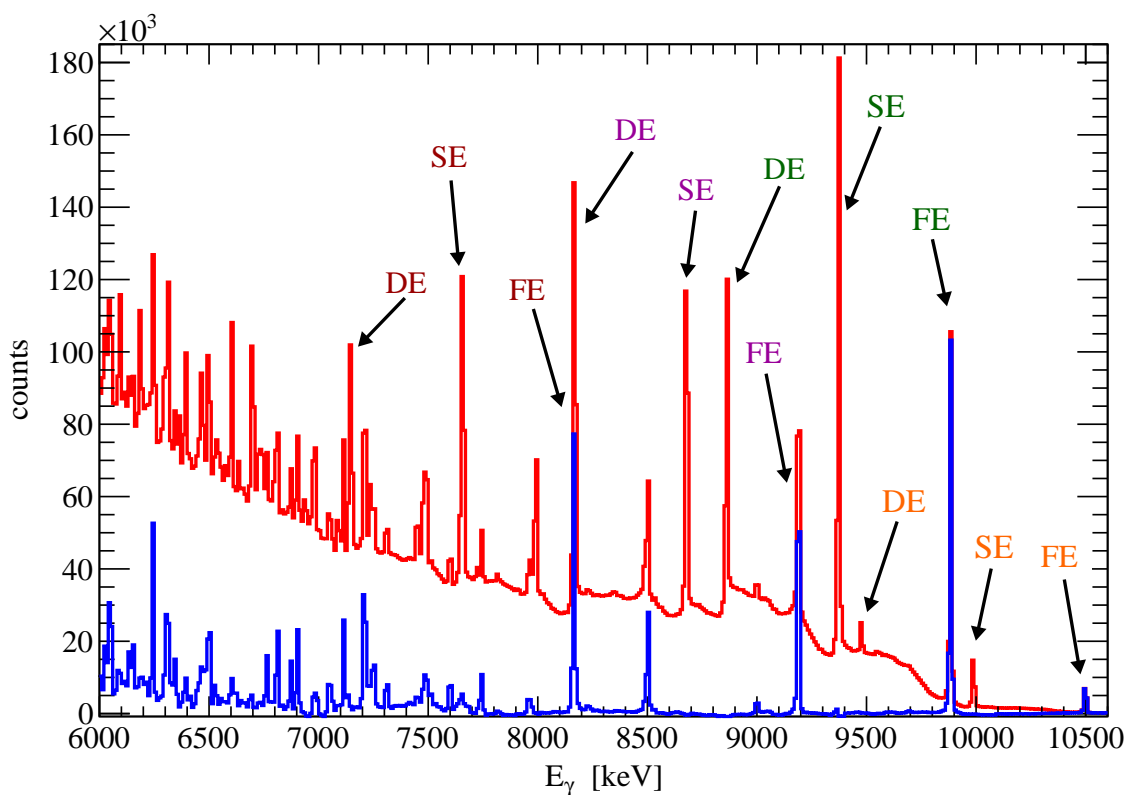


Figure 5.6 – A zoom in figure 5.5. After the response correction only full-energy peaks (FE) remain whereas the single-escape (SE) and double-escape (DE) peaks are fully subtracted.

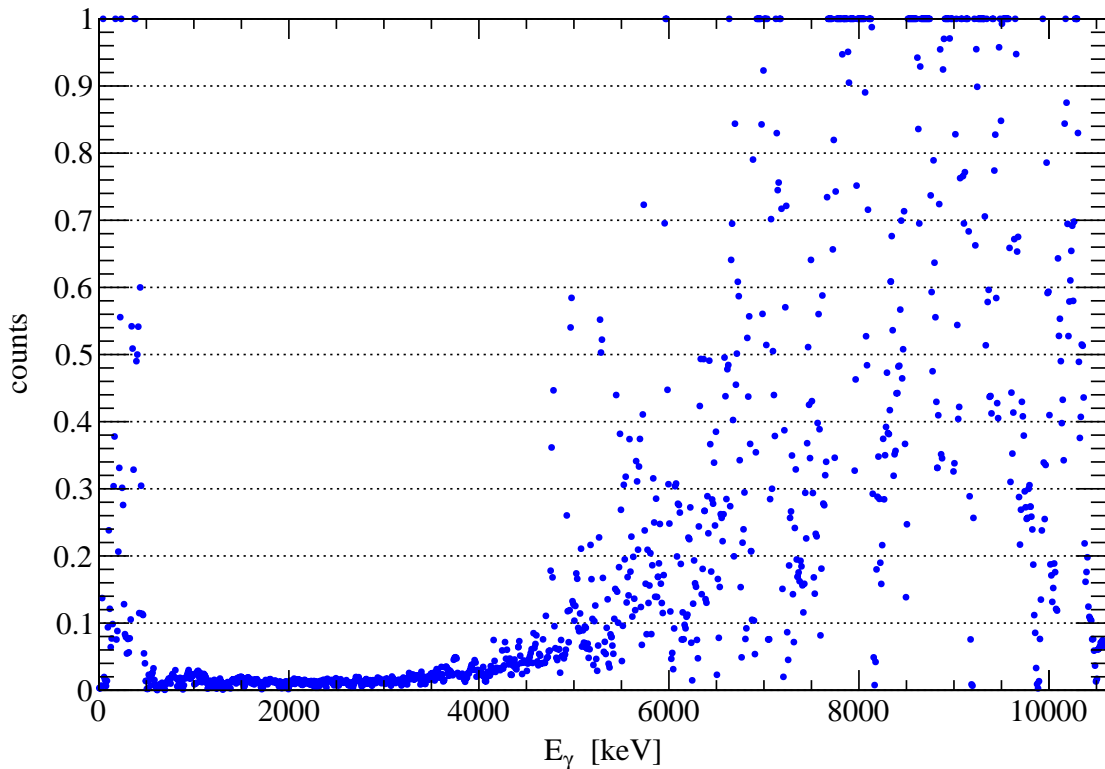


Figure 5.7 – The relative error after the response correction (further explanations in the text).

To estimate the uncertainties of the response corrected spectrum, the measured spectrum and the response matrix have been copied 20 times, whereas the content N_i of each bin i have been randomized based on a Gaussian distribution $\mathcal{G}(N_i, \Delta N_i)$. Then each of the 20 randomized spectra have been response corrected with the 20 randomized response matrices, resulting in 400 different response corrected spectra. The final response corrected spectrum and its uncertainty can be calculated from the mean and standard deviation of these 400 spectra.

At energies above ~ 6 MeV, the relative uncertainty, presented in figure 5.7, is very large for bins containing only Compton continuum. In this region the statistical fluctuations of the bins at higher energies still propagate to low-energy bins, leading to large uncertainties. In combination with bin contents close to zero (which is due to the fully subtracted Compton continuum), this leads to these large relative uncertainties. In contrast, the relative uncertainties of bins containing peaks (e. g. at 9883 keV, 9187 keV and 8170 keV) are only a few percent, because of the higher statistics.

For bins below ~ 6 MeV the correlations between different iterations come into play and start to cancel out fluctuations resulting from previous iterations. Therefore, the response correction stabilizes and for energies between 0.5 and 5 MeV the error is only in the order of the statistical uncertainty (1 to 10%) of the uncorrected spectrum (see 5.4).

This is in favor of the analysis of the quasi-continuum, as this energy range covers its biggest part (see section 5.4). Below 0.5 MeV the response correction does not work properly, because the annihilation peak is not fully subtracted. This is the reason why nearly everything below 0.5 MeV is subtracted.

Due to binning effects, it could happen that artifacts in form of a negative spike followed by a positive spike (or vice versa) with approximately the same height appear where escape peaks have been before. This effect is visualized in figure 5.8. The negative spike has a negative bin content and is skipped by the response correction algorithm. The positive spike instead is wrongly treated like a peak and a response correction is performed. Therefore, an algorithm has been developed that detects and smooths such artifacts before the iteration step is performed (see the red histogram in figure 5.8).

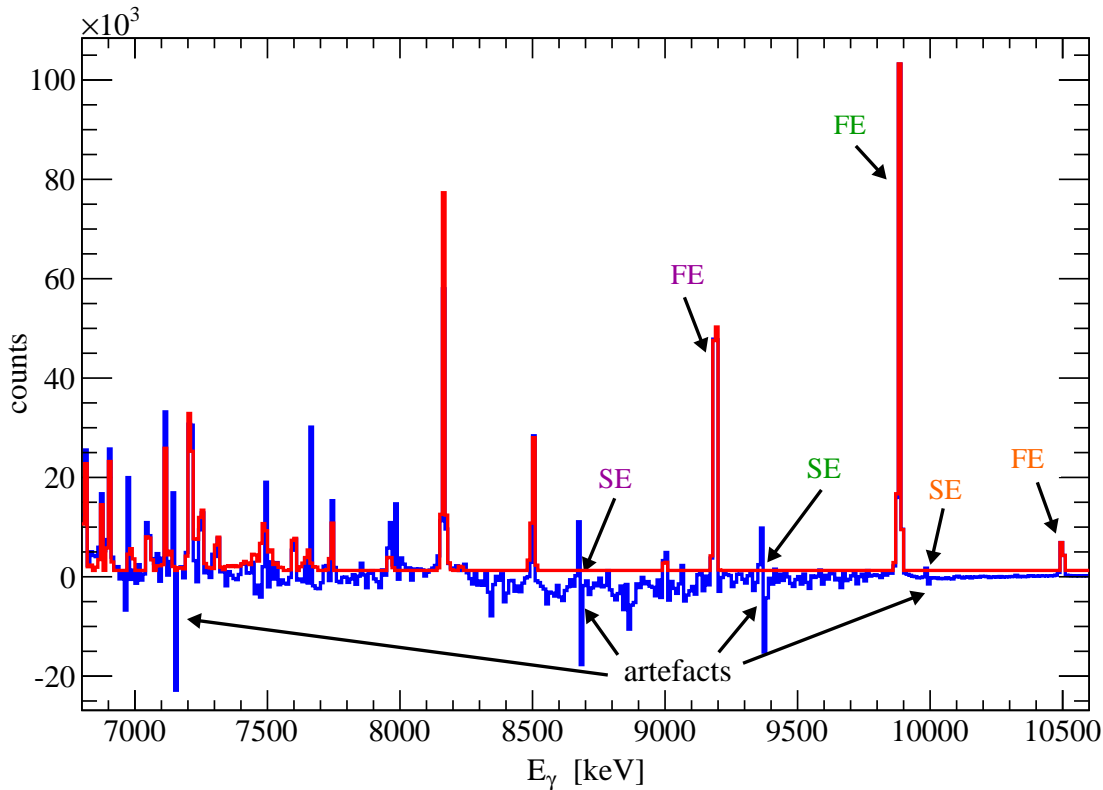


Figure 5.8 – Artefacts occurring after the response correction (blue) due to binning effects. By smoothing those artefacts before the next iteration of the response algorithm is done, the red spectrum is observed. If the smoothing is not applied, the response correction algorithm wrongly subtracts detector response of the positive spike.

5.3 Coincidence Analysis

The creation of coincidence spectra is based on two parameters: a time window, which defines how close in time two events have to be to be treated as coincident, and an energy gate, which selects only those coincidence events, where the energy of one photon is in a certain interval.

The former has been estimated by [John 14]. Therein it has been shown that a time window of 200 ns is the most efficient one. The energy gate has been chosen to be $P \pm 3\sigma$ to cover the peak as much as possible, without including unnecessarily much background. To further reduce the background, two additional gates to the left and right of the peak have been chosen. Then the coincidence spectrum of the background region has been subtracted from the coincidence spectrum of the peak region.

To reduce the time needed to loop over all recorded events, an event-builder has been developed. It groups events that are coincident and saves them in a new file as one coincidence event. It also handles exceptions as it is indicated in table 5.3. Considering an example where three events A , B and C are detected 150 ns one after another, B is coincident with A and C , but A and C are not coincident. The event builder then generates two coincidence events: $(A + B)$ and $(B + C)$. On the one hand no combinations are rejected, on the other hand the event B is counted twice. The time stamps of the newly formed coincidence events is set to the the time stamp of the first detected event in the raw data.

Thanks to this event builder the time for analyzing all coincidence events has been reduced from one day to two hours.

In the $^{77}\text{Se}(n,\gamma)^{78}\text{Se}$ reaction, the transitions from the first excited state at 613.72 keV and the second excited state at 1308.64 keV to the ground state are very prominent. For each of these transitions and each detector combination, coincidence spectra have been generated.

Although the LOHENGRIN and GASP detectors are not suitable for the response correction, all events in which the 613.72 keV or 1308.64 keV gamma-ray was detected by a LOHENGRIN and GASP detector are also taken into account.

In figure 5.9 the high energy part of a coincidence spectrum gated on the transition from the first excited state to the ground state is shown. The resulting spectrum should contain only the gamma rays from transitions that populate the first excited state at 613 keV. As expected, the peak resulting from the de-excitation from the capture state at 10497.76 keV to the ground state vanished, because this transition bypasses the first excited state. The direct transition from the capture state to the

recorded events	time (ns)	\rightarrow	coincidence events	time (ns)
A	0	}	A+B	0
B	150			
C	300		B+C+D	150
D	310			
E	800		E	800
F	1500	}	F+G+H	1500
G	1550			
H	1570			

Table 5.3 – Scheme of how the event builder merges events to coincidence events for time window of 200 ns.

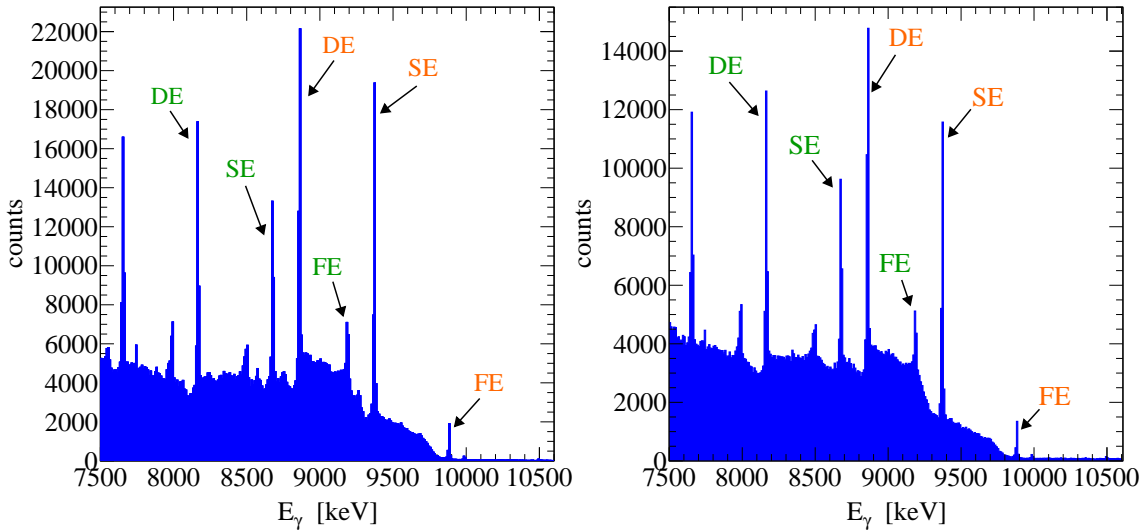


Figure 5.9 – The spectrum of gamma rays coincident to the transition from the first excited state to the ground state. The ratios of escape-peak areas (SE and DE) to the full-energy peak areas (FE) is much larger than in the singles spectra (see fig. 4.11 and 5.6). This appears with the computer code described in the text (left) and with computer code developed by [John 14] (right).

first excited state is visible, which is also as expected. However, when comparing the escape-peak to full-energy peak ratios of the coincidence spectra with those determined in section 4.3, a huge discrepancy appears. Whereas the previously deduced double-escape peak to full-energy peak ratio is around 1 or less, in the coincidence spectrum the double-escape peak is more than ten times larger than the full energy peak. When analyzing the spectra gated on the 1308.64 keV peak and the $^{35}\text{Cl}(n,\gamma)^{36}\text{Cl}$ measurement, the same effect is observed.

This problem has been addressed in the course of a rather time consuming analysis. However, no explanation for this effect has been found so far. In general, it would have been expected that the escape-peak to full-energy peak ratios are the same in singles and coincidence analysis, since their ratio only depends on the detection process in the HPGe crystal. To assure that the computer code used for this analysis is not malfunctioning, the computer code developed for the coincidence analysis in [John 14] has also been used. There a coincidence matrix is generated directly from the energy calibrated TTree. Both computer codes are fully independent, but as shown in figure 5.9 the same effect appears.

Since the two computer codes generate the same results, it suggests itself that this problem emerges from erroneous time stamps in the data. To track down its origin, the problem has been communicated to the EXILL community [Vale S] [Mich C] and is still under investigation.

Unfortunately, this effect hinders the ongoing analysis. When trying to correct the coincidence spectra for detector response, the escape peaks are not subtracted sufficiently because of the small full-energy peak. This leads to an erroneous response subtraction in the following iterations as well.

5.4 Strength Function

The analysis of the quasi-continuum in coincidence spectra is inaccessible due to the problems stated in the previous section 5.3. Nevertheless, it is possible to analyze the measured singles spectra of each EXOGAM detector.

At first, each measured spectrum is corrected for the detector response with the individual response functions estimated with the EXILL simulation (see section 5.2). Subsequently the response-corrected spectra are corrected for the detector efficiencies, which were calculated in section 5.1. When adding up the response and efficiency corrected spectra of each crystal, the spectrum presented in figure 5.10 is obtained. The transitions from the capture state to the ground state and the low lying excited states are very well distinguishable. In the intermediate part of the spectrum the quasi-continuum appears as a broad bump formed of many first, second or even higher order transitions.

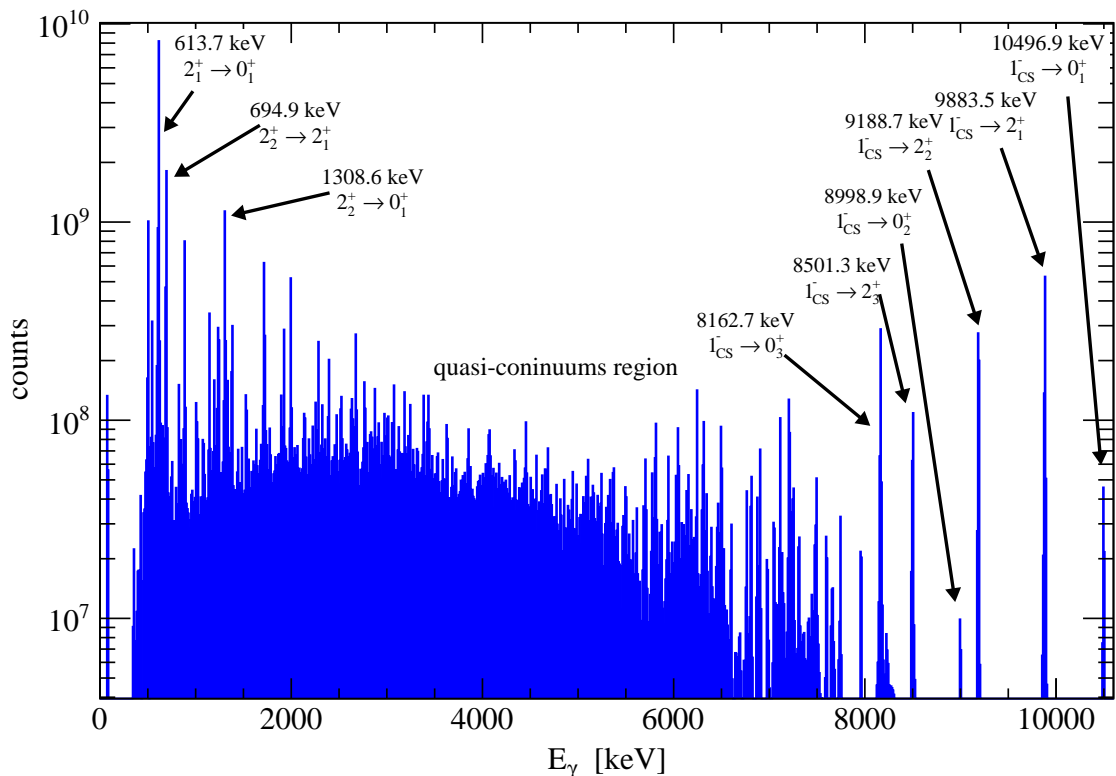


Figure 5.10 – Efficiency and response-corrected spectrum of the $^{77}\text{Se}(n,\gamma)^{78}\text{Se}$ reaction measured with all EXOGAM detectors. The transitions from the low lying excited states to the 0_1^+ ground state are well visible in the low-energy region of the spectrum. The high-energy region is dominated by the transitions from the 1_{CP}^- capture state to the low lying excited states. Between the high and low energy regions, the spectrum is formed of numerous weak transitions, which are visible as a quasi-continuum.

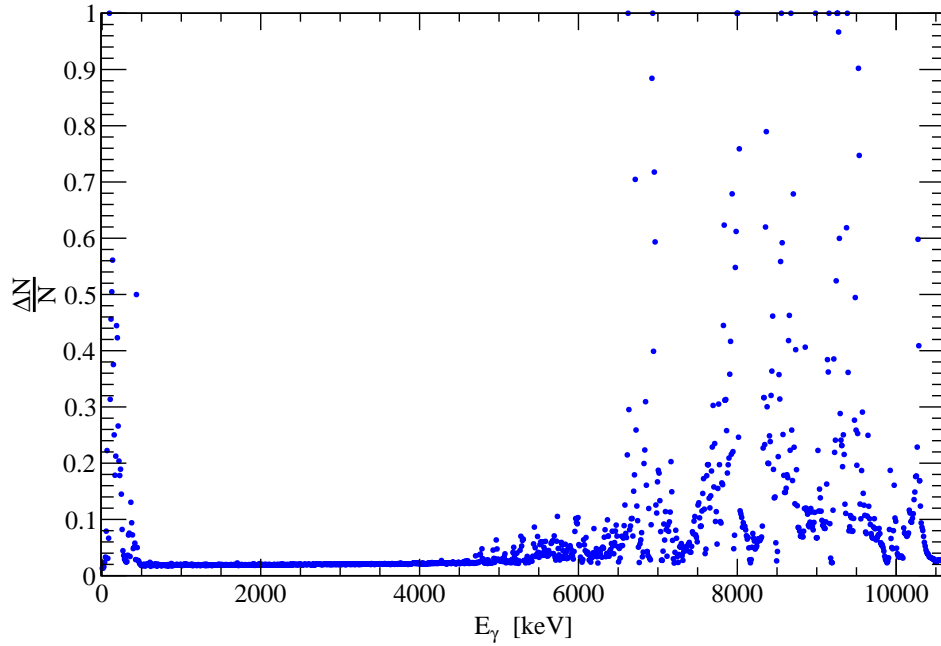


Figure 5.11 – Relative error of the spectrum presented in figure 5.10. In the region of the quasi-continuum the error is in the order of 2 to 3%. At high energies the errors are larger, because of low bin contents (see section 5.2).

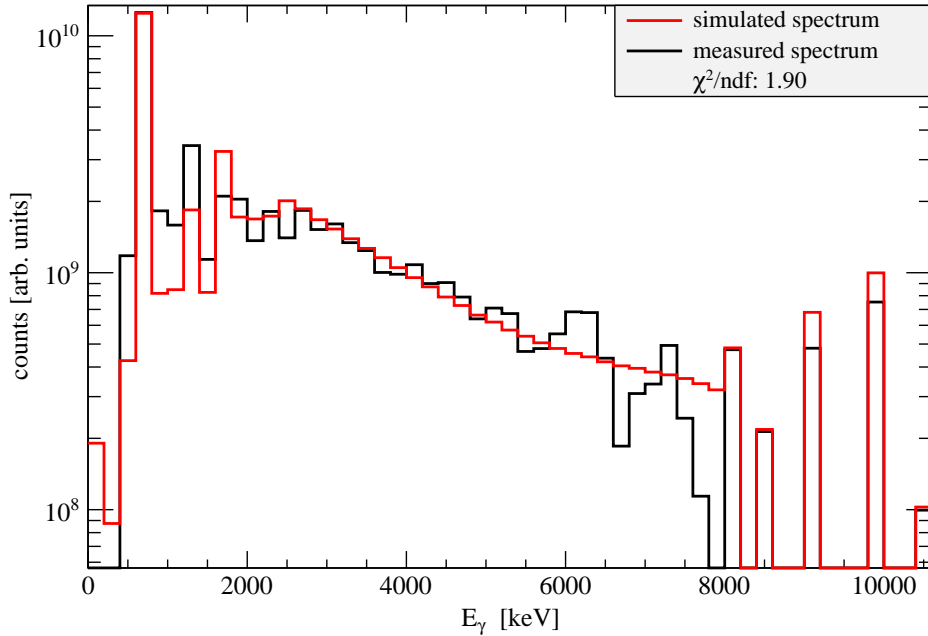


Figure 5.12 – The spectrum presented in figure 5.10 with 200 keV binning in comparison with the spectrum simulated with γ Dex. The best agreement with the experiment was achieved with a temperature of $T = 900$ keV for the CTM level density model, which confirms the results in [Schr 11]. An excess at 6 to 6.4 MeV indicates extra strength which cannot be described by the strength functions implemented in γ Dex. The presented χ^2 value is calculated for the energy range from 2 to 6 MeV.

In figure 5.11 the relative uncertainties of the spectrum in figure 5.10 are shown. In the region of the quasi-continuum, the uncertainties are about 2 to 3% only. For energies above 7 MeV the uncertainties are larger for the same reasons as already explained in section 5.2.

The spectral distribution of the emitted gamma rays was simulated using the statistical code γ Dex [Schr 12] [Mass 14] [Maki 14], that calculates gamma-ray cascades based on an extreme statistical approach. The input parameters discussed in sections 2.3.1 and 2.3.2 were applied. The slope of the average spectra distribution mainly depends on the temperature used in the Constant Temperature Model for the level density. Therefore, several simulations with different temperatures have been performed and compared with the response and efficiency corrected spectrum. To assure the statistical approach, a bin width of 200 keV has been used. In that way the fluctuations in the quasi-continuum region (as present in fig. 5.10) are averaged out and the slope of the quasi-continuum is better distinguishable.

The comparison of simulation and experiment confirms the values of reference [Schr 12]: A temperature of $T_{CTM} = 900$ keV describes the experimentally observed spectrum best (see fig. 5.12). Furthermore, the enhanced yield from 6 to 6.4 MeV confirms the observation of additional strength in this region.

6 Results, Discussion and Outlook

Within the presented thesis a Geant4 simulation of the EXILL detector setup comprising 46 individual HPGe crystals has been developed and evaluated. The evaluation was conducted by comparing experimental and simulated quantities, such as efficiencies, escape-to-full-energy peak ratios and spectra of the ^{152}Eu decay and $^{35}\text{Cl}(n,\gamma)^{36}\text{Cl}$ reaction. It has been shown that simulation and experiment are in a reasonable agreement.

However, after learning the Geant4 framework while developing the EXILL simulation, the insight in the possibilities and features of Geant4 is much grater and a new Geant4 version with more features has been released. Furthermore, in the current version of the simulation all the individual crystals of the EXOGAM clover detectors are described in the same manner, although they exhibit different properties in the experiment. The same applies to the GASP and LOHENGRIN detectors. Another aspect is the detector resolution, which is not yet implemented, as it is due to the complex setup another very time-consuming task.

For these reasons it is desirable to overhaul the simulation code and update to the new Geant4 version, in order to use the new features as well. An extensive benchmark simulation with different parameters is already in process, to determine the properties of each crystal individually. Along with the update, the interactive commands to steer the simulation and the graphical user interface coming along with Geant4 can be designed in a more user-friendly way.

As the EXILL community is very interested in the developed simulation [Gras L], the update will be the first task in the future work following this thesis.

The second goal of the thesis was the investigation of the quasi-continuum of the $^{77}\text{Se}(n,\gamma)^{78}\text{Se}$ reaction. Using the multi-detector array EXILL and a highly enriched ^{77}Se target, it was planned to study coincidence spectra and deduce strength functions on excited states. This goal could not be achieved as expected due to yet unexplained effects after the coincidence analysis (see section 5.3).

The reason for this problem seems to originate from incorrect time stamps in the recorded data. In cooperation with the members from the EXILL community, the problem is under investigation. As soon as the problem is solved, the analysis will be continued because the coincidence analysis in a neutron capture experiment has not been done to such an extent so far. Similar to the previously conducted twin experiment presented in [Schr 12], the results of a successful analysis may contribute new aspects to the discussion of the Axel-Brink hypothesis (see section 2.3.1).

Once the problem is solved it is expected that the analysis will be done in a rather short time, since the computer code for the analysis has been already developed. Furthermore, the event builder presented in 5.3 allows a fast analysis of triple and multi coincidence events.

The whole singles spectrum of the $^{77}\text{Se}(n,\gamma)^{78}\text{Se}$ reaction has been analyzed. Therefore, a response-correction algorithm based on the spectrum-strip method has been developed and successfully applied to the spectra measured with the individual HPGe crystals of the EXOGAM detectors. The response functions were simulated with the aforementioned EXILL simulation.

To correct the spectra for efficiency, the absolute efficiencies of the HPGe detectors were deduced from the experiment using measurements of the ^{152}Eu decay and $^{35}\text{Cl}(n,\gamma)^{36}\text{Cl}$ reaction.

The response and efficiency corrected spectra of the individual crystals have been merged and compared with simulations of the statistical γ -cascade computer code γDex . The best fit was obtained for a temperature of $T = 900\text{ keV}$ in the Constant Temperature Model for the level density. Furthermore, an excess of strength from 6 to 6.4 MeV was found. Both results confirm the findings in [Schr 11].

The developed EXILL simulation and the deduced absolute efficiencies are, beside the good use within this thesis, a valuable basis for the calculation of absolute cross sections and other quantities from measurements conducted in the course the EXILL campaign.

A Appendix

Absolute Efficiencies

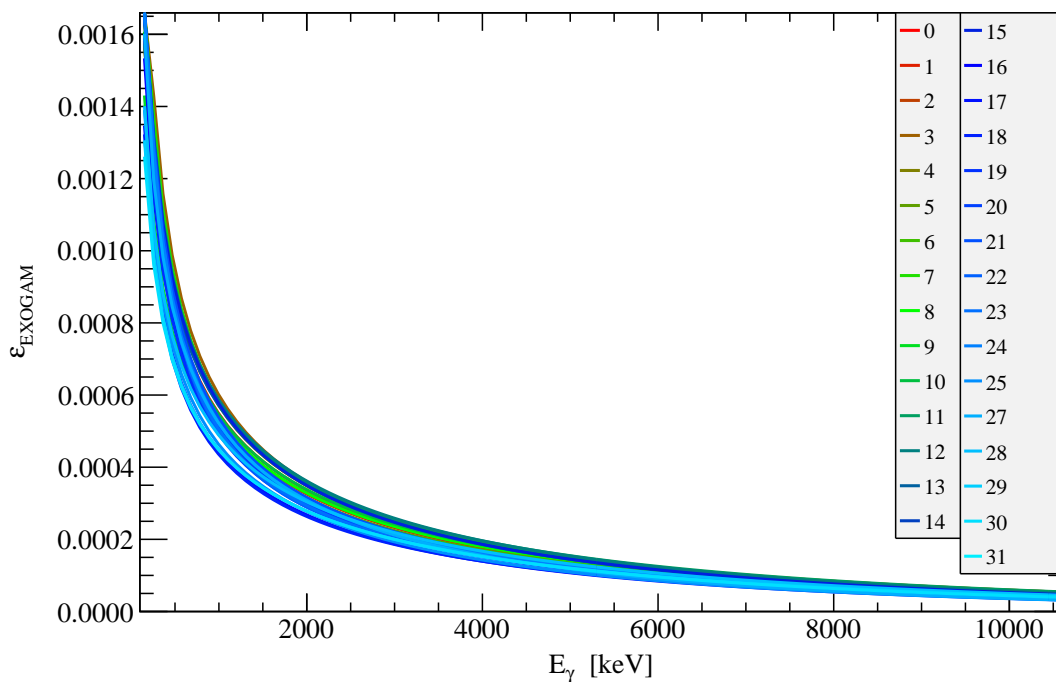


Figure A.1 – The absolute efficiencies of the EXOGAM crystals (102 kBq ^{152}Eu source). The broad distribution of curves shows how the properties of the individual crystals fluctuate. Between some crystals the efficiencies differ by 20 %.

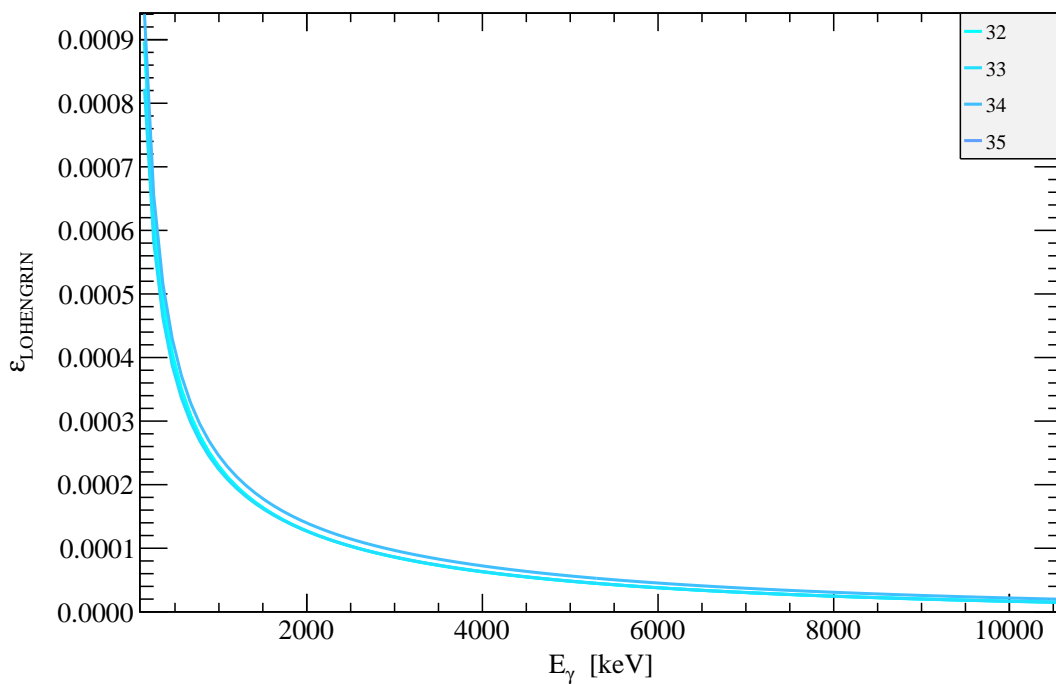


Figure A.2 – The absolute efficiencies of the LOHENGRIN crystals (102 kBq ^{152}Eu source). The efficiencies are lower than those from the EXOGAM crystals, because of the smaller crystal size.

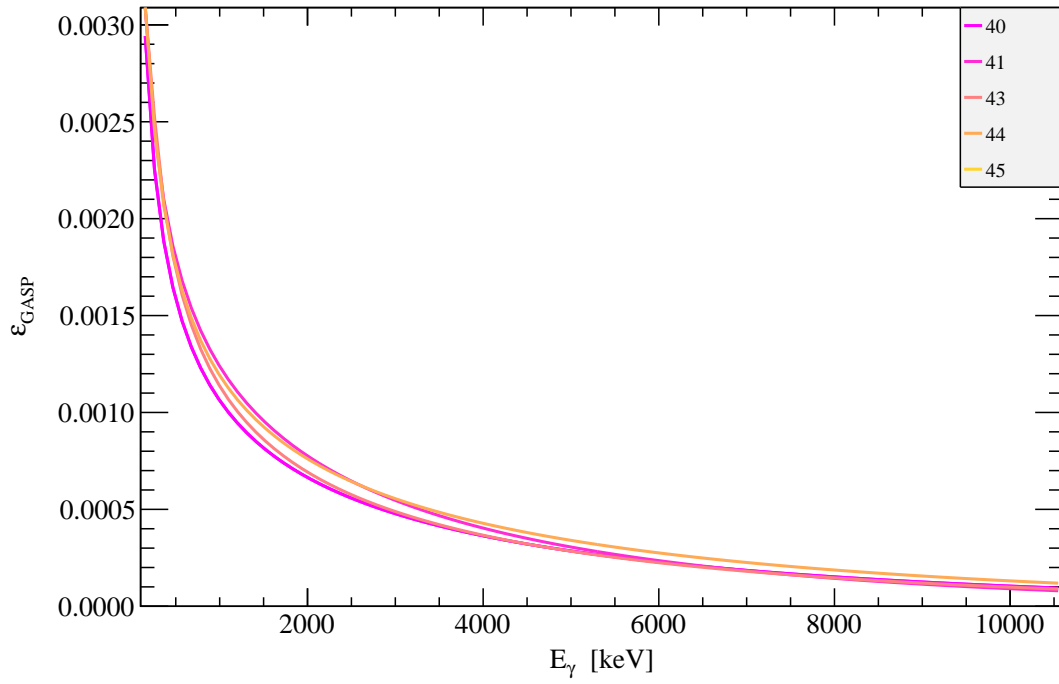


Figure A.3 – The absolute efficiencies of the GASP crystals (102 kBq ^{152}Eu source). The efficiencies are higher than those from the EXOGAM crystals, because of the much larger single crystals.

References

- [Al Q 03] S. Al-Quraishi, S. Grimes, T. Massey, and D. Resler. “Level densities for $20 \leq A \leq 110$ ”. *Physical Review C*, Vol. 67, p. 015803, 2003.
- [Alva 93] R. Alvarez, C. “The GASP Array”. *Nuclear Physics News*, Vol. 3, No. 3, 1993.
- [Audi G 04] 2004. <http://amdc.in2p3.fr/masstables/Ame2003/rct7.mas03>.
- [Axel 62] P. Axel. “Electric Dipole Ground-State Transition Width Strength Function and 7-Mev Photon Interactions”. *Physical Review*, Vol. 126, p. 671, 1962.
- [Bart 73] G. A. Bartholomew, E. D. Earle, A. J. Ferguson, J. W. Knowles, and M. A. Lone. *Gamma-Ray Strength Functions*, p. 229. Vol. 7, Springer US, 1973.
- [Bazz D] private communication. [Dino Bazzacco](#), INFN, Sezione di Padova, I-35122 Padova, Italy.
- [Brin 55] D. M. Brink. “Some aspects of the interaction of fields with matter”. 1955. PhD thesis, Oxford University.
- [Burg 83] D. Burgess, D. and J. Tervo, R. “Background Estimation for Gamma-Ray Spectrometry”. *Nuclear Instruments and Methods*, Vol. 214, p. 431, 1983.
- [Egid 05] T. von Egidy and D. Bucurescu. “Systematics of nuclear level density parameters”. *Physical Review C*, Vol. 72, p. 044311, 2005.
- [Egid 09] T. von Egidy and D. Bucurescu. “Experimental energy-dependent nuclear spin distributions”. *Physical Review C*, Vol. 80, p. 054310, 2009.
- [ENSDF] 2014. <http://www.nndc.bnl.gov/ensdf/>.
- [Evan 72] D. Evans, R. *Gamma Rays*. McGraw-Hill, 1972.
- [EXO GAM] 2003. <http://pro.ganil-spiral2.eu/laboratory/detectors/exogam>.
- [GASP] 1990. <http://npgroup.pd.infn.it/GASP/pictures/HPGe.jpg>.
- [Geant4] S. Agostinelli, J. Allison, K. Amako, J. Apostolakis, H. Araujo, P. Arce, M. Asai, D. Axen, S. Banerjee, G. Barrand, F. Behner, L. Bellagamba, J. Boudreau, L. Broglia, A. Brunengo, H. Burkhardt, S. Chauvie, J. Chuma, R. Chytracsek, G. Cooperman, G. Cosmo, P. Degtyarenko, A. Dell’Acqua, G. Depaola, D. Dietrich, R. Enami, A. Feliciello, C. Ferguson, H. Fesefeldt, G. Folger, F. Foppiano, A. Forti, S. Garelli, S. Giani, R. Giannitrapani, D. Gibin, J. J. Gómez Cadenas, I. González, G. Gracia Abril, G. Greeniaus,

W. Greiner, V. Grichine, A. Grossheim, S. Guatelli, P. Gumplinger, R. Hamatsu, K. Hashimoto, H. Hasui, A. Heikkinen, A. Howard, V. Ivanchenko, A. Johnson, F. W. Jones, J. Kallenbach, N. Kanaya, M. Kawabata, Y. Kawabata, M. Kawaguti, S. Kelner, P. Kent, A. Kimura, T. Kodama, R. Kokoulin, M. Kossov, H. Kurashige, E. Lamanna, T. Lampén, V. Lara, V. Lefebure, F. Lei, M. Liendl, W. Lockman, F. Longo, S. Magni, M. Maire, E. Medernach, K. Minamimoto, P. Mora de Freitas, Y. Morita, K. Murakami, M. Nagamatu, R. Nartallo, P. Nieminen, T. Nishimura, K. Ohtsubo, M. Okamura, S. O’Neale, Y. Oohata, K. Paech, J. Perl, A. Pfeiffer, M. G. Pia, F. Ranjard, A. Rybin, S. Sadilov, E. Di Salvo, G. Santin, T. Sasaki, N. Savvas, and e. a. Sawada, Y. “Geant4—a simulation toolkit”. *Nuclear Instruments and Methods in Physics Research Section A: Accelerators, Spectrometers, Detectors and Associated Equipment*, Vol. 506, p. 250, 2003.

- [Gera 92] A. Gerasimov, S. “Simple Method for Background Subtraction in Gamma-ray Spectra”. *International Journal of Radiation Applications and Instrumentation. Part A. Applied Radiation and Isotopes*, Vol. 43, No. 12, p. 1529, 1992.
- [Gilib 65] A. J. Gilbert and G. W. Cameron, A. “A Composite Nuclear-Level Density Formula With Shell Corrections”. *Canadian Journal of Physics*, Vol. 43, p. 1446, 1965.
- [Gras L] private communication. [Dr. Laura Grassi](#), INFN, Sezione di Padova, I-35122 Padova, Italy.
- [Gros 05] A. A. Gros, S. “*Characteristion of an EXOGAM Clover Germanium Detector*”. Doktorarbeit, 2005. PhD thesis, University of Liverpool.
- [Heyd 10] K. Heyde, P. von Neumann-Cosel, and A. Richter. “Magnetic dipole excitations in nuclei: Elementary modes of nucleonic motion”. *Reviews of Modern Physics*, Vol. 82, p. 2365, 2010.
- [Huy 10] Q. Huy, N. “The influence of dead layer thickness increase on efficiency decrease for a coaxial HPGe p-type detector”. *Nuclear Instruments and Methods in Physics Research A*, Vol. 621, p. 390, 2010.
- [ILL PF1B] 2012. <http://www.ill.eu/instruments-support/instruments-groups/instruments/pf1b/description/instrument-layout/>.
- [ILL RE] 2006. <http://pd.chem.ucl.ac.uk/pdnn/inst3/reactors.htm>.
- [Jent M] private communication. [Dr. Michael Jentschel](#), Institut Laue-Langevin, 38042 Grenoble, France.

- [John 14] R. John. “Untersuchung von Gammakaskaden und Stärkefunktionen in der Neutroneneinfangsreaktion $^{77}\text{Se}(n,\gamma)$ ”. 2014. Diploma thesis, Technische Universität Dresden.
- [Jung 08] A. R. Junghans, G. Rusev, R. Schwengner, A. Wagner, and E. Grosse. “Photon data shed new light upon the GDR spreading width in heavy nuclei”. *Physics Letters B*, Vol. 670, p. 200, 2008.
- [Kawa 76] Y. Kawarasaki. “A Simple Method for Generation of Background-Free Gamma-Ray Spectra”. *Nuclear Instruments and Methods*, Vol. 133, p. 335, 1976.
- [Klei 28] O. Klein and Y. Nishina. “Über die Streuung von Strahlung durch freie Elektronen nach der neuen relativistischen Quantendynamik von Dirac.”. *Zeitschrift für Physik*, Vol. 52, p. 853, 1928.
- [Knol 10] F. Knoll, G. *Radiation Detection and Measurement*. John Wiley & Sons, Inc., 4th Ed., 2010.
- [Koni 08] A. J. Koning, S. Hilaire, and S. Goriely. “Global and local level density models”. *Nuclear Physics A*, Vol. 810, p. 13, 2008.
- [Kope 93] J. Kopecky, M. Uhl, and R. E. Chrien. “Radiative strength in the compound nucleus ^{157}Gd ”. *Physical Review C*, Vol. 47, p. 312, 1993.
- [Kost U] private communication. [Dr. Ulli Köster](#), Institut Laue-Langevin, 38042 Grenoble, France.
- [Lang H] private communication. [Dr. Hans Juergen Lange](#), CANBERRA GmbH, D-65428 Rüsselsheim, Germany.
- [Maki 14] A. Makinaga, R. Massarczyk, R. Schwengner, M. Beard, F. Dönnau, M. Anders, D. Bemmerer, R. Beyer, R. Hannaske, R. Junghans, A. M. Kempe, T. Kögler, M. Röder, K. Schmidt, and A. Wagner. “Dipole strength of ^{181}Ta for the evaluation of the ^{181}Ta stellar neutron capture rate”. *Physical Review C*, Vol. 90, p. 044301, 2014.
- [Mart 06] F. Martin. “Étude des distributions en masse, charge nucléaire et énergie cinétique des produits de fission de l' $^{233}\text{U}(n_{\text{th}},f)$ et du $^{241}\text{Pu}(n_{\text{th}},f)$ mesurées auprès du spectromètre de masse Lohengrin (ILL)”. 2006. PhD thesis, Université de Grenoble.
- [Mass 14] R. Massarczyk. “The effect of neutron excess and nuclear deformation on dipole strength functions below the neutron separation energy - nuclear resonance fluorescence experiments on $^{124,128,132,134}\text{Xe}$ at ELBE and HI γ S”. 2014. PhD thesis, Technische Universität Dresden.
- [Maye 02] T. Mayer-Kuckuk. *Kernphysik: Eine Einführung*. Teubner Studienbücher, Vieweg+Teubner Verlag, 7th Ed., 2002.

- [MCNP] X-5 Monte Carlo Team. “MCNP—A General Monte Carlo N-Particle Transport Code, Version 5”. *Los Alamos National Laboratory*, Vol. LA-UR-03-1987, 2003.
- [Mene R] private communication. [Dr. Roberto Menegazzo](#), INFN, Sezione di Padova, I-35122 Padova, Italy.
- [Mich C] private communication. [Dr. Caterina Michelagnoli](#), GANIL, 14000 Caen, France.
- [Mugh 06] S. Mughabghab. *Atlas of Neutron Resonances: Resonance Parameters and Thermal Cross Sections. Z=1-100*. Elsevier Science, 2006.
- [Mutt 13] P. Mutti, A. Blanc, G. de France, M. Jentschel, U. Köster, R. Martinez, M. G. Simpson, T. Soldner, A. Ur, C. and W. Urban. “A Trigger-less Acquisition System for the EXILL Large Germanium Detectors Array”. *Advancements in Nuclear Instrumentation Measurement Methods and their Applications (ANIMMA), 2013 3rd International Conference on*, 2013.
- [Radf 87] C. Radford, D. I. Ahmad, R. Holzmann, V. F. Janssens, R. and L. Khoo, T. “A Prescription for the Removal of Compton-Scattered Gamma Rays from Gamma-Ray Spectra”. *Nuclear Instruments and Methods in Physics Research A*, Vol. 258, p. 111, 1987.
- [RIPL3] <http://www-nds.iaea.org/RIPL-3/>.
- [ROOT] R. Brun and F. Rademakers. “ROOT - An Object Oriented Data Analysis Framework”. *Nuclear Instruments and Methods in Physics Research Section A: Accelerators, Spectrometers, Detectors and Associated Equipment*, Vol. 389, p. 81. <http://root.cern.ch/>.
- [Schm 11] K.-H. Schmidt and B. Jurado. “Thermodynamics of nuclei in thermal contact”. *Physical Review C*, Vol. 83, p. 014607, 2011.
- [Schr 11] G. Schramm. “Analysis and Simulation of Photon Scattering and Neutron Capture Gamma Spectra”. 2011. Diploma thesis, Technische Universität Dresden.
- [Schr 12] G. Schramm, R. Massarczyk, A. R. Junghans, T. Belgya, R. Beyer, E. Birgersson, E. Grosse, M. Kempe, Z. Kis, K. Kosev, M. Krtička, A. Matic, K. D. Schilling, R. Schwengner, L. Szentmiklósi, A. Wagner, and J. L. Weil. “Dipole strength in ^{78}Se below the neutron separation energy from a combined analysis of $^{77}\text{Se}(n,\gamma)$ and $^{78}\text{Se}((\gamma,\gamma'))$ experiments”. *Physical Review C*, Vol. 85, p. 014311, 2012.
- [Simp 00] J. Simpson, F. Azaiez, G. deFrance, J. Fouan, J. Gerl, R. Julin, W. Korten, J. Nolan, P. M. Nyakó, B. G. Sletten, M. Walker, P. and the EXOGAM Collaboration. “The EXOGAM Array: A Radioactive Beam Gamma-Ray Spectrometer”. *Acta Physica Hungarica*, Vol. 11, p. 159, 2000.

[Vale S] private communication. [Stanislav Valenta](#), Charles University, 116
36 Prague 1, Czech Republic.

Danksagung

Ich allein hätte es bis hierhin, bis zur Vollendung des Studiums gewiss nicht schaffen können, stünde mir nicht seit jeher meine Familie mit Rat und Tat, alten Weisheiten und Ausgewogenheit zur Seite. Dafür möchte ich meinen Eltern und Großeltern herzlichst danken. Meinem Bruder danke dafür, dass er mir ein ruhiger und friedliebender Mitbewohner während der Zeit des Studiums (und auch davor) war. Ich danke meiner geliebten Freundin Nataša, die mir stets Motivation ist weiter zu machen bei allem was ich tu und die mein Leben täglich aufs Neue bereichert.

Weiterhin bedanke ich mich bei allen Kollegen für die warme und hilfsbereite Atmosphäre in der ersten Etage des Gebäudes 620 des HZDR. Allen voran gebührt der Dank meinem Betreuer Ronald Schwengner, der immer da war, wenn man ihn brauchte, Ralph Massarczyk, den ich mit nervigen und sich wiederholenden Fragen quälen konnte ohne seine Missgunst auf mich zu ziehen, Arnd Junghans, der meine Fragen ausgiebigst beantwortete auch wenn er keine Zeit hatte, und nicht zuletzt Professor Thomas Cowan und Andreas Wagner, dank denen ich meine Arbeit am HZDR anfertigen konnte.

Auch bedanke ich mich bei Manfred Sobiella, der viel Zeit investiert hat, für mich die CAD-Datei aufzuarbeiten und Toni Kögler für viele Tipps und Tricks.

Physik ist (noch) nicht alles, daher danke ich Stefanie Todt und Alexander Schneider für die vielen Badminton Abende, und Roland Hannaske, der meine Begeisterung für Floorball weckte.

Erklärung

Hiermit versichere ich, dass ich die vorliegende Arbeit ohne unzulässige Hilfe Dritter und ohne Benutzung anderer als der angegebenen Hilfsmittel angefertigt habe. Die als fremde Quellen direkt oder indirekt übernommenen Gedanken sind als solche kenntlich gemacht. Die Arbeit wurde bisher weder im Inland noch im Ausland in gleicher oder ähnlicher Form einer anderen Prüfungsbehörde vorgelegt.

Die vorgelegte Arbeit wurde am Helmholtz-Zentrum Dresden-Rossendorf, Institut für Strahlenphysik, im Zeitraum von Oktober 2013 bis November 2014 angefertigt.

Christian Lorenz
Dresden, 20. November 2014

